Texas A&M University
Mechanical Engineering Department
Turbomachinery Laboratory
Tribology Group

REVAMPING AND PRELIMINARY OPERATION OF A THRUST BEARING TEST RIG

Research Progress Report to TAMU Turbomachinery Research Consortium

TRC-B&C-02-2015

By
Luis San Andrés
Mast-Childs Chair Professor
Principal Investigator

Michael Rohmer
Research Assistant

Scott Wilkinson
Research Assistant

May 2015

Year II

A TEST RIG FOR EVALUATION OF THRUST BEARINGS AND SEALS

TRC Project, TEES # 32513/1519F2

Executive Summary

Progress in the revamping and operation of a thrust bearing test rig follow. After a catastrophic failure in 2013 when operating with air radial bearings, a concerted effort has brought the test rig into an operating condition with water-lubricated bearings. Ref. [1] details the failure and several repairs and modifications. In 2014-15, students completed revamping the test rig; it is ready for measurements! Modifications included manufacturing two rotors, repairing the main housing, aligning the motor shaft and test rotor, upgrading the water pipeline system, envisioning a static/dynamic load system, installing instrumentation, and developing means of data acquisition. Presently, the revamped system has rotated to a speed of 5 krpm.

Measurements of the free-free mode natural frequencies and lateral mode shapes of the rotor-coupling system show that the rotor and quill shaft operate as a unit. Once assembled, water lubricated the bearings to lift and support the test rotor connected to the motor through its coupling. Impact loads identify the system fundamental natural frequency and damping ratio for operation without rotor speed or active thrust bearings. The flexibility of the quill shaft commands the location of the system lateral natural frequency (~ 93 Hz) and its low damping ratio. XLTRC^2 based predictions agree well with the measured natural frequency and identified damping ratio. Further measurements with an increasing static load on the test thrust bearing under pure hydrostatic conditions (no shaft rotation) evidence the film axial clearance increases as the water supply pressure, max. 4.14 bar(g). As the imposed axial load increases, the operating clearance decreases exponentially as also the thru flow rate decreases while the pocket pressure increases.

In the next year, measurements of the static and dynamic load performance of a water lubricated hybrid thrust bearing will continue with planned tests with shaft rotation. The test rig could also be used to test oil or gas lubricated thrust bearings (7.62-cm outer diameter) at a maximum shaft speed of 9 krpm and with an applied load up to 750 N.

Note: The USAF Upper Stage Technology Program (2006-2009) funded the design, construction and operation of a test rig for performance measurement of water lubricated hybrid thrust bearings. Water also lubricates the radial bearings supporting the rotor, hydrostatic/hydrodynamic type

Table of Contents

List of Tables

List of Figures

Introduction

In rotating machinery, thrust bearings support axial loads and control shaft position. In turbomachinery, such as axial compressors, axial loads depend on both shaft speed and operating pressure. The prediction of (impeller) axial loads is largely empirical, creating the need for reliable thrust bearings [2]. To enhance thrust bearing technology, Texas A&M University (TAMU) designed and built a thrust bearing test rig to supply reliable experimental results to validate predictive tools [3].

USAF (2006-2009) funded a project to design and construct a water lubricated thrust bearing test rig to measure the forced performance of hybrid thrust bearings operating at high supply pressure and high rotational speed. The measurements from the test hybrid thrust bearings exhibited remarkable correlation with results from a predictive tool [4].

In 2013, the thrust bearing test rig, modified to operate with air lubricated radial bearings, experienced large amplitude vibrations leading to severe damage with loss of parts [1]. The test rig, currently fully revamped to operate with water as a lubricant, will provide reliable experimental results for various types of thrust bearings.

This report provides a brief literature review on hydrostatic thrust bearings, a description of the revamping process of the test rig, and measurements made on a water lubricated hybrid thrust bearing during preliminary operation without shaft rotation. As work continues, the test rig will be used to measure the static and dynamic performance of the water lubricated hybrid thrust bearing. The test rig can be easily be to measure the force performance of other thrust bearing types and face seals, for example.

A Review of Hydrostatic Thrust Bearings

Background

Hybrid (hydrostatic/hydrodynamic) thrust bearings (HTBs) are common in rotating machinery applications that require a high centering stiffness and accurate rotor positioning, such as precision machine tools, gyroscopes, telescopes, process fluid pumps, and other turbomachinery including cryogenic turbo pumps [5]. HTBs use an externally pressurized fluid to support (without contact) an axial load whereas hydrodynamic thrust bearings rely on shaft rotational speed to generate a hydrodynamic pressure supporting the load. Some other advantages of HTBs include a high load capacity, high damping coefficients, and no contact of bearing surfaces at low surface speeds. The load capacity, stiffness, and damping coefficients of a HTB depend on the lubricant supply

pressure and the thrust collar rotational speed. Therefore, if more stiffness or load capacity are required, the supply pressure could be increased (at the expense of an increase in flow rate).

Principle of Operation of a Hydrostatic Bearing

Rowe (1983) [6] describes the principle of operation of hydrostatic bearings. The fluid flow in a hydrostatic bearing overcomes two modes of flow resistance: first, the lubricant flows through a flow restrictor (orifice, capillary, constant flow valve) before coming into a recess, then it flows from the recess across a small clearance film land region. As the clearance decreases, the flow rate reduces, thus reducing the frictional head loss through the orifice. Hence, the recess pressure increases, albeit never to exceed the supply pressure (with the exception of a hydrodynamic pressure in a shallow pocket). As the recess pressure increases, the fluid pressure generates a higher reaction load between the rotor and bearing causing them to separate. Contrarily, if the axial clearance increases, the flow rate and pressure drop through the orifice also increase causing the recess pressure to decrease. As the recess pressure decreases, the fluid pressure generates a lower reaction load between the rotor and bearing causing the rotor move toward the bearing. It is by this means that a hydrostatic bearing generates a stiffness.

Effects of Geometry and Flow Restriction Type on HTB Performance

The geometry of the recess and the compensating flow element (orifice, capillary, constant flow valve) largely influence the performance of HTBs. Figure 1 shows four common HTB geometries. Sternlicht and Elwell (1960) [7] derive closed form design equations for the flow rate and load capacity of a single circular recess HTB and an annular multi-recess HTB, verifying their accuracy against experimental results. The authors test both a single circular recess HTB and an annular HTB (4 recesses) using various means of flow restriction. The annular HTB has a much higher load capacity and stiffness than the single recess HTB at the same pocket pressure. HTBs with a capillary restriction have the lowest stiffness while HTBs with a constant flow restriction have the highest stiffness. Also, HTBs with a capillary restriction have a load capacity and stiffness that are independent of fluid viscosity, whereas HTBs with a constant flow rate restriction have a load capacity and stiffness that are independent of supply pressure. However, once the HTB with a constant flow restriction begins to exceed its maximum specific load (load/area), the bearing stiffness experiences a sharp cut off where it drops from its peak magnitude to zero.

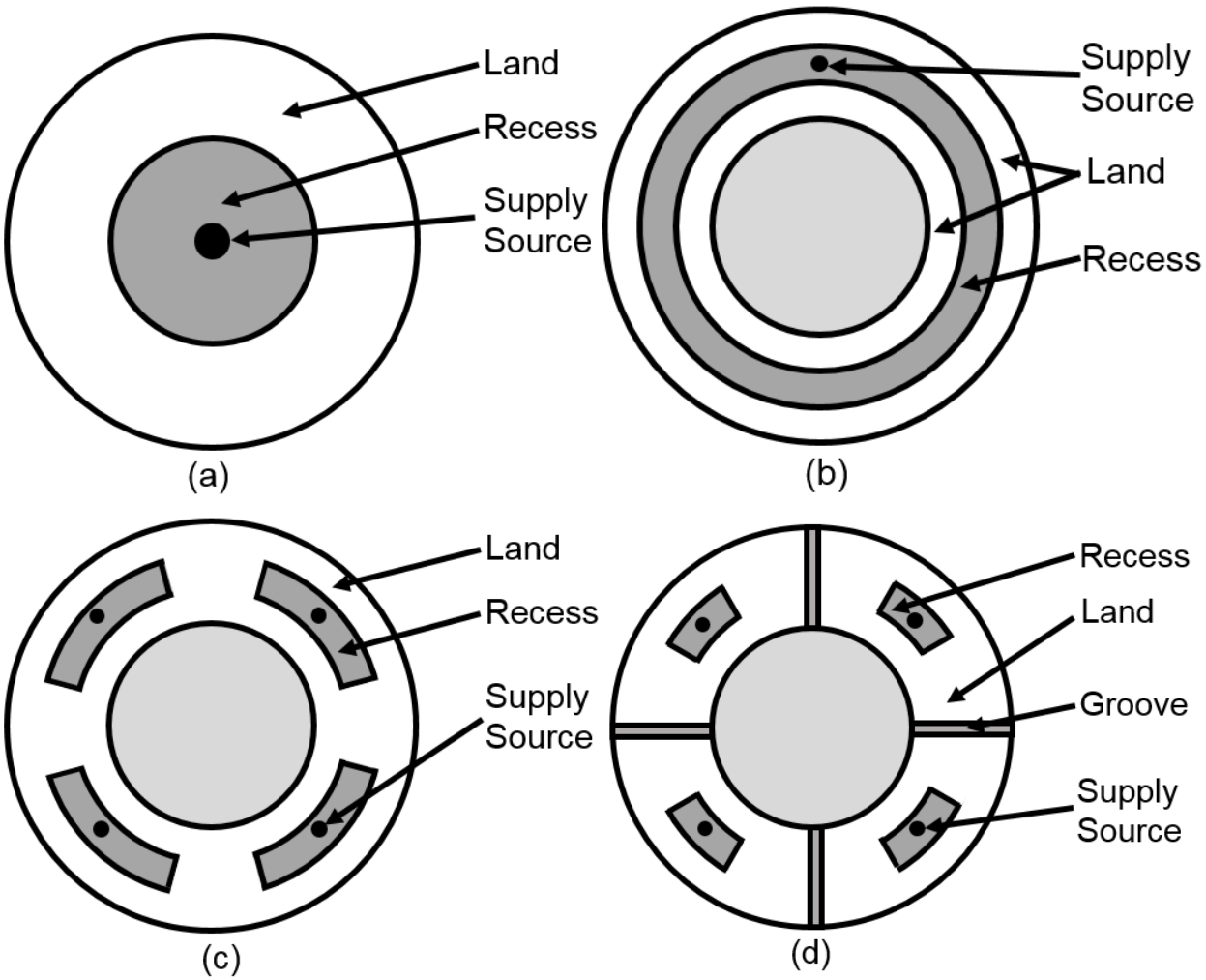

Figure 1. Common recess geometries in HTBs, including: (a) single circular recess thrust bearing, (b) annular groove thrust bearing, (c) annular multi-recess thrust bearing, and (d) multi-pad thrust bearing.

Rowe (1983) [6] calculates the load and flow rate for an incompressible fluid lubricated HTB; analytically for simple geometries such as the single circular recess HTB, and computationally for complex geometries. Rowe [6] shows annular groove HTBs demand a higher flow rate and provide a higher load capacity than a single circular recess HTB. Multi-recess HTBs have a similar load capacity and flow rate as an annular groove HTB. The multiple recess HTB produces a restoring torque when the rotor and bearing surfaces are not parallel.

High Performance Thrust Bearings for High Speed Applications

Cryogenic fluid turbo pumps operate with high shaft speed and a large pressure difference. A feasible method of rotor support is to implement hybrid (hydrostatic/hydrodynamic) fluid bearings.

Hybrid fluid bearings offer an economically attractive and reusable alternative to ultra-precision ceramic ball bearings, as they have no surface speed limitation or *DN* (diameter x rotor speed) limit. The advantages of hybrid bearings enable a turbo pump to be smaller, lighter, and operating with an increase in mechanical efficiency. The following references present test data to validate the performance of high-speed, high-pressure HTBs [8].

San Andrés (2000) [8] performs a bulk-flow analysis to predict the performance of a multi-recess, orifice-compensated, angled injection HTB. The application relates to cryogenic fluid turbo pumps that experience a high shaft speed (180 krpm) and a large pressure difference (550 bar). As the applied load increases, the film clearance decreases causing a decrease in flow rate and increase in recess pressure. The stiffness coefficient has an optimum value when there is a 40% pressure drop across the orifice (recess pressure is 60% of supply pressure). The damping coefficient increases as the clearance decreases or the rotational speed increases while the drag torque increases with either rotational speed or clearance. At high rotor speed and low load, centrifugal flow fluid inertia plays a significant role as it may cause fluid starvation through the bearing inner diameter and suction pressures just downstream of the edge of the recesses. The model accounting for fluid inertia at both the recesses and the film lands shows a higher damping coefficient and a lower dynamic stiffness coefficient than the model only accounting for fluid inertia at the recesses. Fluid inertia on the bearing film land has a large effect on the bearing performance characteristics.

San Andrés (2002) [9] follows with a computational analysis to predict the performance of HTBs with angular misalignment for cryogenic fluid turbo pumps operating at a rotor speed of 180 krpm ($\mathrm{Re}_C = \rho_S \Omega R_{out} C / \mu_S = 33,000$ where ρ_S and μ_S are the fluid density and viscosity, Ω is the shaft rotational speed, R_{out} is the bearing outer radius, and C is the nominal film clearance). The static and dynamic axial stiffness as well as the static and dynamic moment-angle stiffness coefficients have a peak magnitude when the recess pressure ratio is approximately 0.6. The axial damping coefficient, the direct moment-tilt angle damping coefficient, and the cross-coupled moment stiffness coefficients slightly increase with load for low to moderate load and then increase rapidly with load for large load due to the large hydrodynamic effect at low clearance. As the misalignment angle increases, variations in recess pressure and film pressure increase, causing the overall mass flow to decrease as less flow exits through the inner diameter. In addition, both moment angle and force axial stiffness coefficients increase as the misalignment angle increases. However, the axial force and the drag torque are largely independent of the collar misalignment

angle. The whirl frequency ratio (for conical rotor motions) is equal to 0.5, thus showing HTBs do not offer any added stability when compared to hydrodynamic thrust bearings.

Forsberg (2008) [3] designs and builds a test rig for water-lubricated HTBs and conducts tests with a non-rotating, HTB (8 pockets) operating with a supply pressure ranging from 3.45 bar to 17.24 bar. Figure 2 shows a cross-sectional view of the test rig, with two-flexure pivot, tilting pad radial hydrostatic bearings supporting the test rotor. The test rig uses two HTBs; a test thrust bearing and a slave thrust bearing. Both face the outer side of the thrust collars of the rotor. The slave thrust bearing is affixed rigidly to a bearing support, as shown on the right of Figure 2. A shaker delivers an axial load (static and/or dynamic) to the test thrust bearing through a non-rotating load shaft. Two aerostatic radial bearings support the axial load shaft with minimal friction for controlled displacement along the axial direction. The test thrust bearing, depicted at the center of Figure 2, moves axially to impose a load on the rotor thrust collar. The slave thrust bearing reacts to the imposed axial load [10].

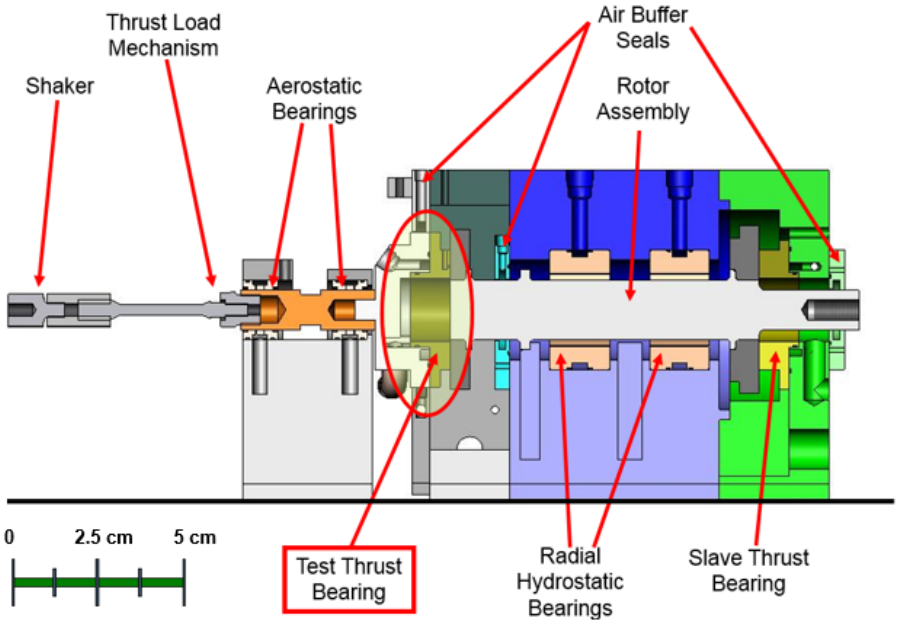

Figure 2. Cross sectional view of thrust bearing test rig [10].

Forsberg [3] finds that the fluid supply pressure has a small influence on the pocket pressure ratio (ratio of pocket pressure to supply pressure). However, the pocket pressure ratio decreases significantly as the operating clearance increases (due to a smaller load) because the lubricant experiences a higher flow rate leading to a higher pressure drop across the orifice. As the supply pressure increases or the clearance decreases, the HTB develops higher pocket pressures that lead

to a higher load capacity and stiffness. Most importantly, the flow rates exiting the bearing through the inner diameter and at the outer diameter are different, which could cause fluid starvation with shaft rotation. The predictions, based on a model in Ref. [9], for both the flow and load agree with measured data within 20%. However, larger discrepancies exist between the predictions and measurements of axial stiffness because of persistent misalignment of the thrust collar faces.

Ramirez (2008) [11] continues Forsberg's work to test a water-lubricated, 8 pocket HTB (8 pockets) operating at a rotor speed ranging from 7.5 krpm to 17.5 krpm and with a supply pressure ranging from 3.45 bar to 17.24 bar. The rotor speed does not have a large effect on the bearing static stiffness or load capacity, indicating a primarily hydrostatic operation. Similar to the non-rotating condition [2], both the load and the static axial stiffness increase as either the supply pressure increases or the clearance decreases due to the higher recess pressure. Flow rate measurements through the inner diameter show the onset of fluid starvation at high rotor speed and low load due to centrifugal fluid flow acceleration. The measurements of inlet flow rate, discharge flow rate through the inner diameter, load capacity, and recess pressure ratio (ratio of recess pressure to supply pressure) differ from predictions by 1%, 5%, 7%, and 10%, respectively.

Esser (2010) [4] continues tests to determine the effect of orifice diameter (1.67 mm, 1.80 mm, 1.93 mm) on the performance of a water lubricated, eight pocket HTB. To this end, Esser conducts tests with the bearing operating at a rotor speed varying from 7.5 krpm to 17.5 krpm, and a supply pressure ranging from 3.45 bar to 17.24 bar. At a given load and supply pressure, the HTB experiences an increase in stiffness and enlarged operating clearance as the orifice diameter increases. While operating at a constant supply pressure, larger orifice diameter and clearance cause the supply flow rate and the exhaust flow rate through the inner diameter to increase, thus mitigating fluid starvation on the bearing inner side. When the orifice diameter increases from 1.80 mm to 1.93 mm, the thrust bearing experiences limited gains in operating clearance and axial stiffness but still requires a much higher flow rate. Overall, the predictions correlate well with measured inlet flow rate, discharge flow rate through the inner diameter, recess pressure, clearance, and axial stiffness coefficient.

San Andrés *et.* al. (2008) [10] report on the test and predictions for the performance of a HTB operating at a rotor speed of 17.5 krpm (surface speed=50 m/s) and a water lubricant supply pressure of 1.72 MPa. At a constant rotor speed, an increase in load or decrease in supply pressure causes a reduction in film clearance and flow rate. On the other hand, with a constant supply

pressure, the rotor speed has little influence on the operating clearance. As the rotor speed increases and the bearing supply pressure decreases, less lubricant flows out through the inner diameter of the thrust bearing causing lubricant starvation. Most importantly, with a rotor spinning, while the thrust bearing operates at a constant supply pressure and rotor speed, the discharge flow rate through the inner diameter rapidly decreases when the load decreases (axial clearance increases) due to centrifugal flow effects. Overall, the predictive tool estimates well the inlet flow rate, exhaust flow rate through the inner diameter, load, and film clearance when compared to measured data recorded for increasing load.

Revamping the Thrust Bearing Test Rig

Appendix A gives a full description of the thrust bearing test rig. Rohmer and San Andrés in a TRC Report (2014) [1] describe the failure of the test rig when operating with air bearings, as well as initial component repairs or replacements such as coating the rotor surface, replacing the journal bearings, removing the damaged surface of the slave thrust bearing, and modifying the air buffer seals. Ref. [1] also details the installation of a water supply system to regulate and measure the pressure and flow rate of the water supplied to the radial and axial bearings.

The following section describes additional repairs and modifications such as:

- Determining the orthogonality of the thrust collar faces.
- Repairing damaged fastener connections on the housing and air buffer seals.
- Enlarging the pipe diameter of the water manifold.
- Aligning the rotor centerline with the motor shaft centerline.
- Designing a static load system.
- Installing instrumentation and developing means of data acquisition.

Rotor

Presently, a 75-μm thick hard chrome coating resurfaces the rotor surfaces damaged during the failure [2]. However, the thrust collar faces appeared not to be orthogonal with the centerline of the shaft. A simple apparatus helps to gain insight to the severity of the misalignment.

Figure **3** shows the rotor resting on a V-block (precision machining equipment for machining angles); three eddy current sensors face a thrust collar to measure the relative axial displacement at three circumferential locations; and hence, aid to determine the collar planar orientation relative to the rotor main axis of rotation. Two eddy current sensors face the rotor and measure the lateral displacement at two locations to determine its axis of rotation. The rotor slowly rotates (by hand) to twelve angular positions, at which the eddy current sensors measure the distance to the test thrust collar. The ad-hoc apparatus does not impose an axial restraint that could prevent the gap between the thrust collar and the three eddy current sensors from changing. The measurement only concerns with the relative axial displacement at various circumferential positions to determine the relative planar orientation (tilt about X and Y axes).

Figure 4 shows the tilt (slope in mm/m) of the test thrust collar about the X and Y axes vs. angular position. The graph includes the axial slope of the shaft, which, found to be a constant, shows the V-block effectively restrains the rotor from laterally translating while rotating. In Figure

4, the tilt about the *Y*-axis trails the tilt about the *X*-axis by 90° but has equal amplitude (demonstrated by a 90° phase shift of the data in Figure 4). The tilt (δ) of the test thrust collar has a peak-to-peak amplitude of nearly 3 mm/m resulting in a peak-to-peak deviation ($R\delta$) of 150 µm at the edge of the thrust collar (R=5.1 cm). The data shows that the test thrust collar is not perpendicular with the centerline of the rotor, most likely the shaft bent during the failure incident.

The evidence of a bent shaft supported the decision to manufacture another rotor. Figure 5 shows a photograph of a newly manufactured rotor to replace the damaged rotor (cost: $4,935). The new rotor has the same basic dimensions as the original rotor. However, it includes some minor details for ease of manufacturing and installation, as well as some holes for insertion of setscrews that act as imbalance masses, if needed.

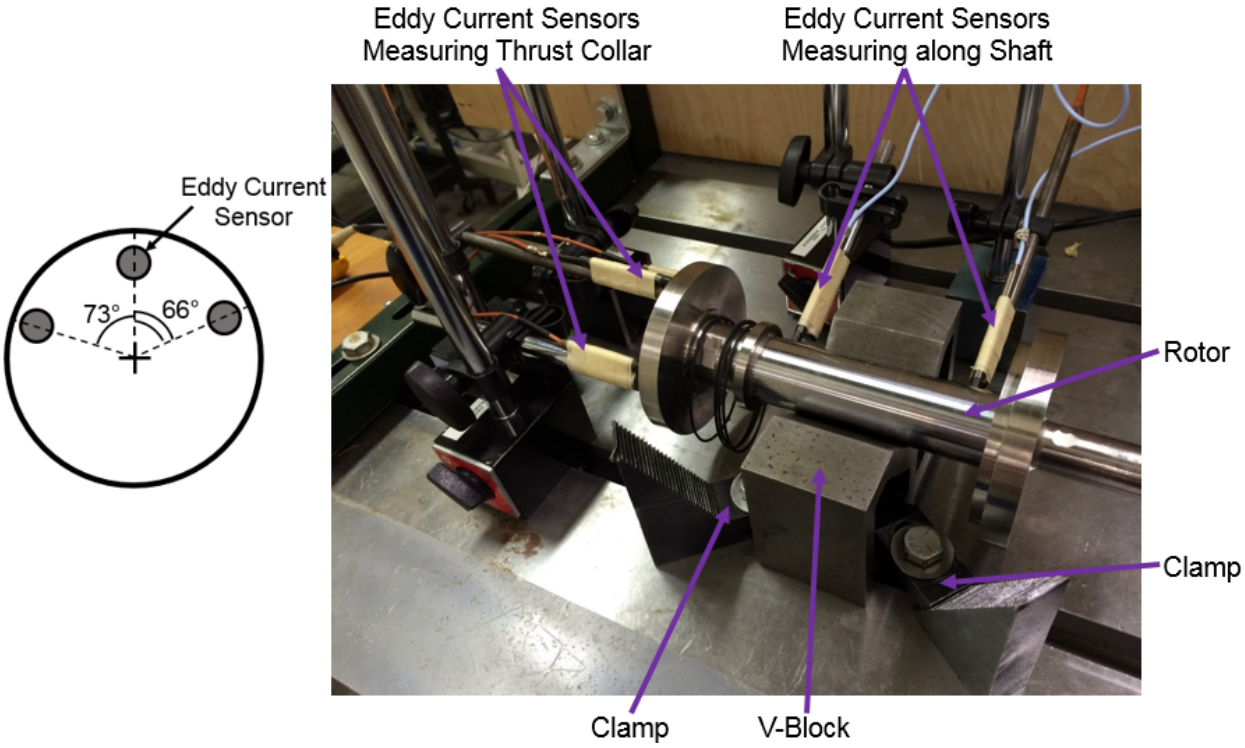

Figure 3. Photograph of rotor resting on a V-block. Three eddy current sensors measure the axial displacement of the test thrust collar at three different locations (shown on inset) to determine its planar orientation. Two eddy current sensors measure the lateral displacement of the shaft to determine its axial orientation.

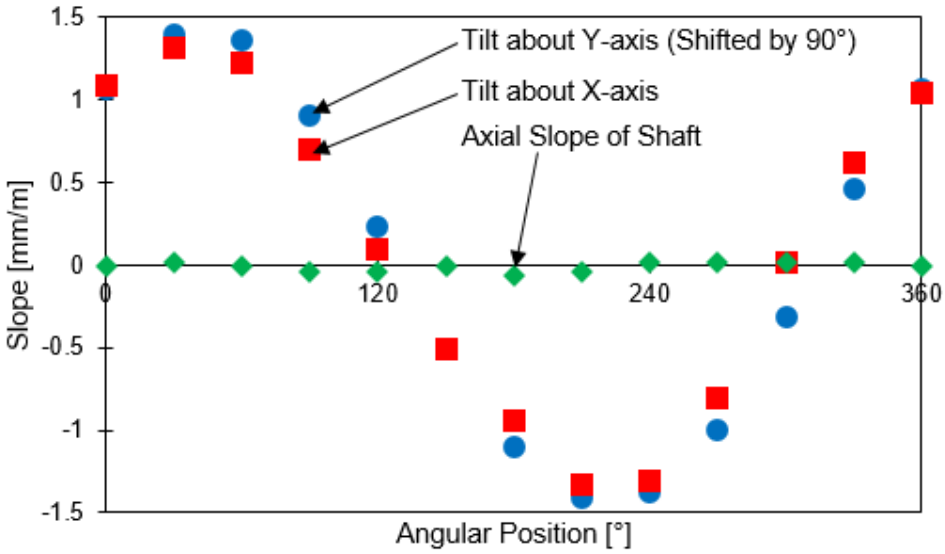

Figure 4. Tilt of the original rotor test thrust collar about the *X* and *Y* axes vs. angular position. The tilt about the *Y*-axis is shifted by 90°. Rotor supported on a V-block. Rotor overall length = 26 cm, thrust collar outer diameter= 10.2 cm.

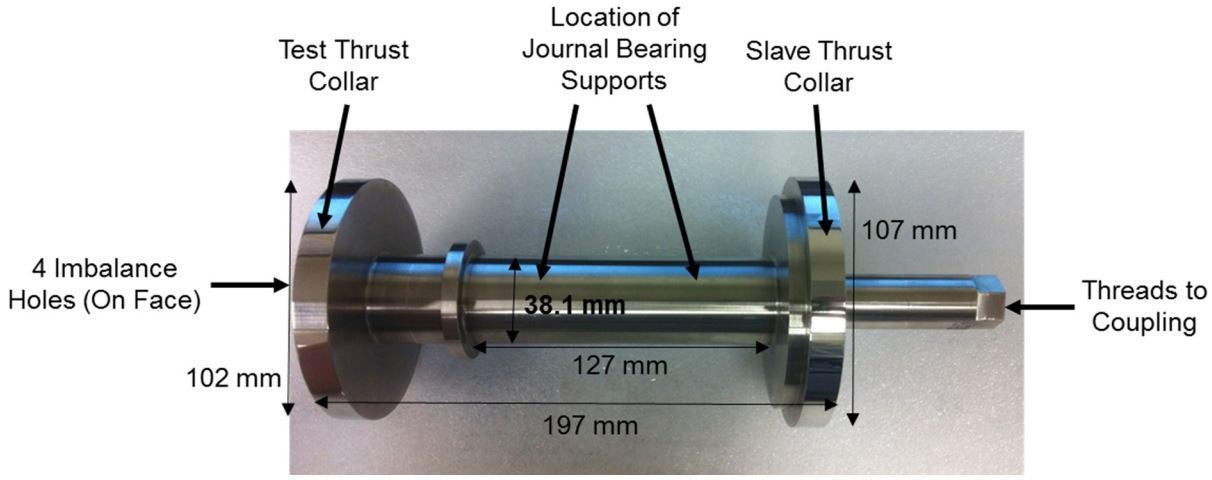

Figure 5. Photograph of manufactured rotor (2014).

Air Buffer Seals and Housing

TRC Report (2014) [1] describes the repair of various individual components but does not address the damage to the housing that holds the air buffer seals and eddy current sensors.

Figure 6 shows a photograph of a side of the housing with both an air buffer seal and an eddy current sensor installed. When the air buffer seals sheared off from the housing, the remnants of the bolts remained in the housing. In addition, the contact between the rotor and eddy current sensors induced large stresses on the threads of the housing that kept the eddy current sensors stationary. A drill/tap process removed the remnant material from the threaded holes.

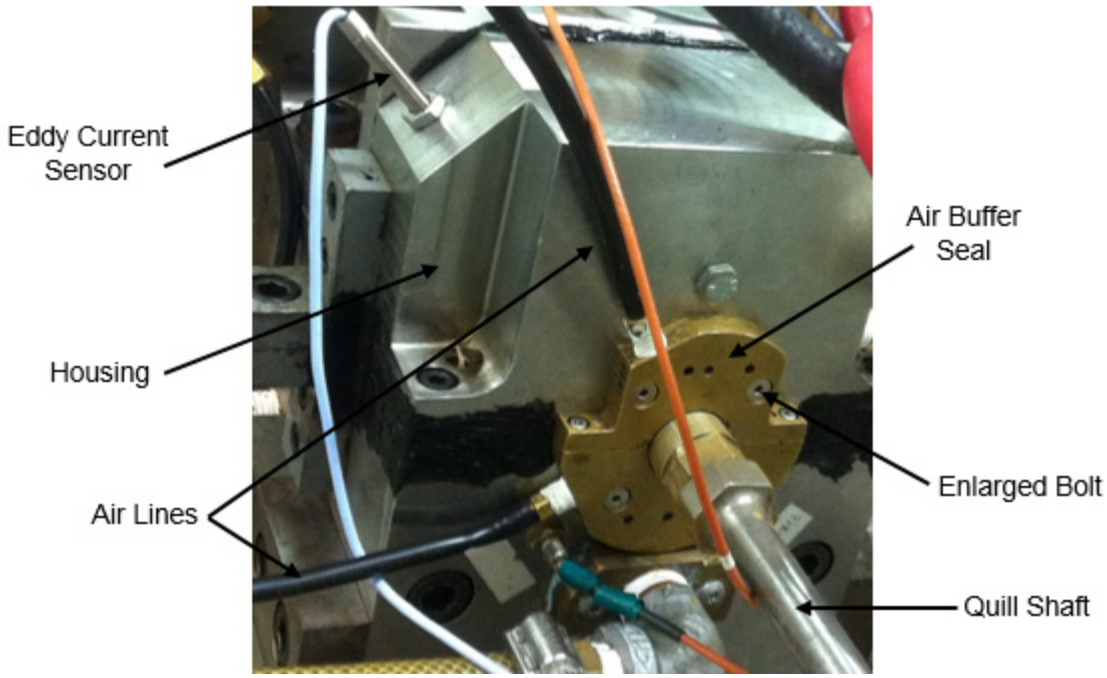

Figure 6. Photograph of air buffer seal and eddy current sensor attached to main housing (after repair in 2015).

Water Manifold

TRC Report (2014) [1] describes the installation of a ¼-inch diameter water manifold to deliver water to the bearings at a regulated pressure. The supply lines, shown in Figure 7, caused a large pressure drop from the main (house water) delivery source to the supply pressure into the bearings. Fluid frictional losses in the original water manifold are especially apparent when the thrust bearings operate with a large axial clearance that demands of a large fluid flow rate.

Fluid frictional losses in a pipe are proportional to the fluid speed squared. At a constant fluid flow rate, the fluid velocity is inversely proportional to the area; therefore, fluid frictional losses decrease as pipe diameter increases. By increasing the pipe diameter to ¾-inch, the fluid velocity decreases to 11% of its original speed, and the fluid pressure loss across the water manifold drops to 1% of the loss associated with the original water manifold configuration. In order to mitigate frictional losses, evidenced by the significant pressure drop, the water delivery system to the bearings was increased to ¾-in pipe diameter, as depicted in Figure 8.

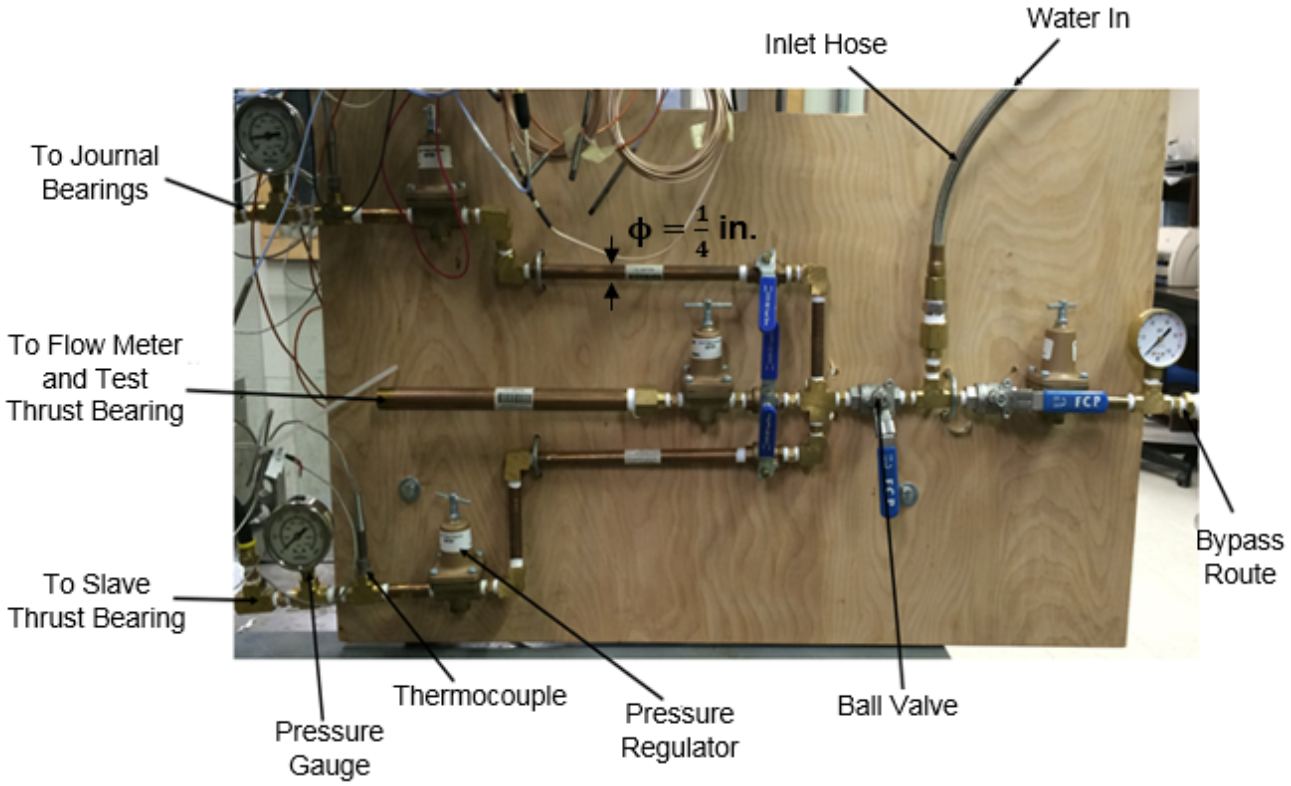

Figure 7. Photograph of original pipelines and manifold for water distribution to bearings (ϕ=1/4 in.).

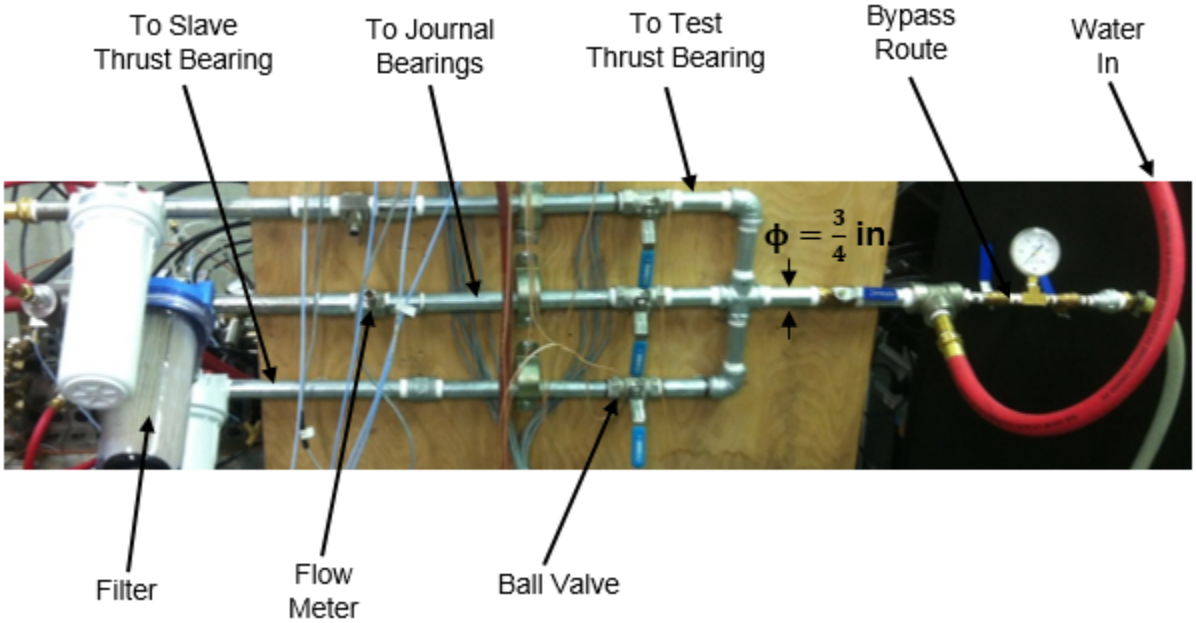

Figure 8. Photograph of modified pipelines and manifold for water distribution to bearings (ϕ=3/4 in.).

Test Rig Assembly

The quill shaft of the coupling threads into the rotor with an installation torque of 278 Nm as per the manufacturer specification. The rotor rests on the bottom halves of the radial bearings. Next, the top and bottom halves of the radial bearings fasten to each other, and O-rings wrap around on the bearings' outer diameter. The top part of the housing fastens to its bottom, and the slave and test thrust bearing housings fasten to complete the test rig assembly. The test thrust bearing and load shaft make an integral assembly. This assembly slides on two aerostatic bearings that are secured to a pedestal. The quill shaft attaches to the remainder of the coupling, a diaphragm and hub that connect to the drive motor.

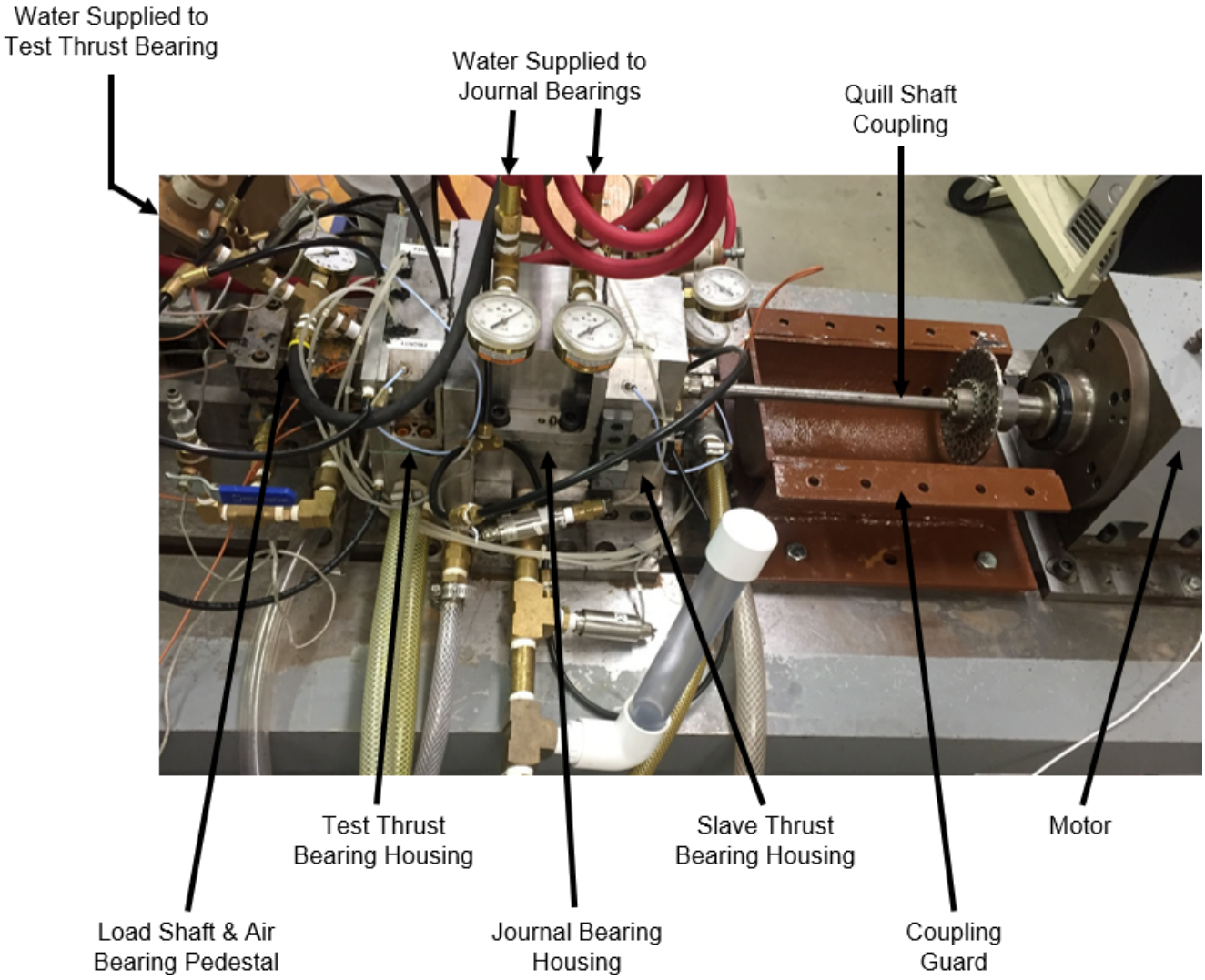

Figure 9. Photograph of the assembled test rig.

Alignment of Motor Shaft and Rotor

With the test rig fully assembled, water at the anticipated operating supply pressure (3.45 bar) feeds the journal bearings and lifts the rotor. Figure 10 shows two tip displacement gauges, mounted on the motor shaft, indicating on the face and rim of the coupling quill shaft. The motor shaft and the rotor slowly turn together (by hand), and the gauges measure the relative displacement of the face and rim at both horizontal and vertical directions. The displacements on the rim and face determine the offset misalignment and the angular misalignment, respectively. Next, a meticulous process displaces the housing to align the motor shaft centerline to the rotor centerline. Once both centerlines align within tolerance, water at various supply pressure (2 – 6 bar(g)) feeds the journal bearings to ensure the alignment remains within tolerance.

Equation (1) shows the alignment tolerance (A = 0.0105 in./in.) between the rotor and motor shaft required for the coupling, as per manufacturer specifications,

$$\frac{x}{L} + \frac{y}{M} \leq A \tag{1}$$

Above, x is the total indicator reading on the rim, y is the total indicator reading on the face, M = 1.328 in. is the distance between indicator measurement and shaft centerline, L = 5.503 in. is the distance between hinge points (specified by coupling vendor), and A is the allowable angular misalignment.

Load System on Test Rig

The rig needs a load system able of applying static and/or dynamic loads onto the thrust bearing. The electromagnetic shakers deliver only a dynamic load, hence the need for a separate static load system. Figure 11 shows the mechanism designed to superimpose the static and dynamic loads. A threaded rod applies a tensile force on a soft spring to rotate the tip of a bar pivoting about a fulcrum (pivot rod). The other end of the bar, amplifies the input load, pushes on a strain gauge load cell connected to the load shaft that holds the thrust bearing. The static load system allows space for a shaker to apply its dynamic load to the load shaft. Due to the stiffness and elastic deformation limit of the (selected) spring, the static load system currently has a maximum load capacity of 900 N. However, the load capacity can increase, as needed.

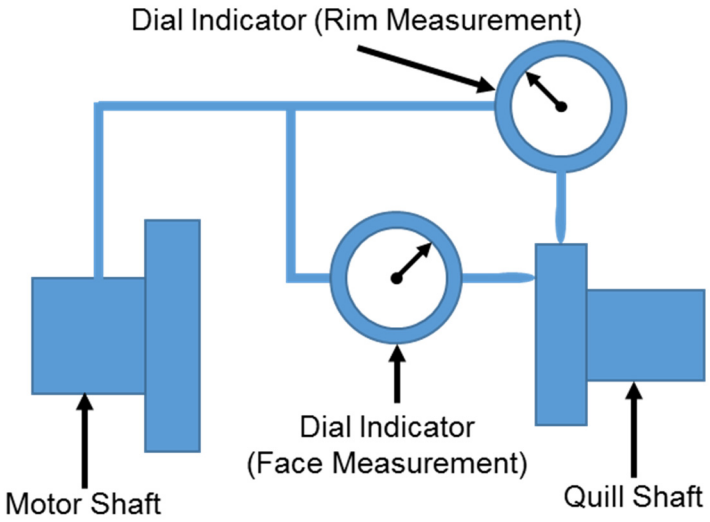

(a)

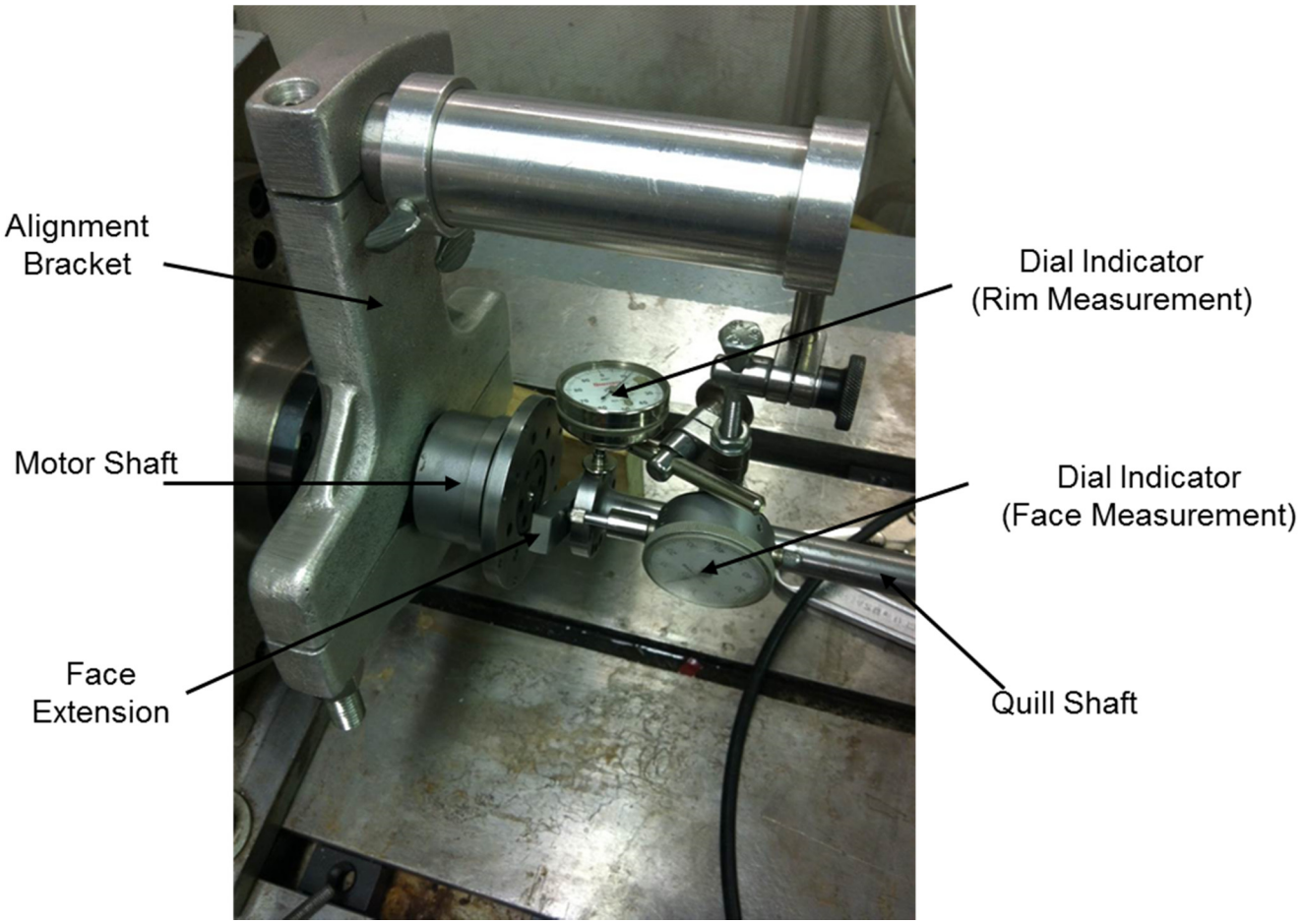

(b)

Figure 10. Schematic (a) and photograph (b) of face and rim alignment method for aligning motor shaft and rotor/coupling quill shaft.

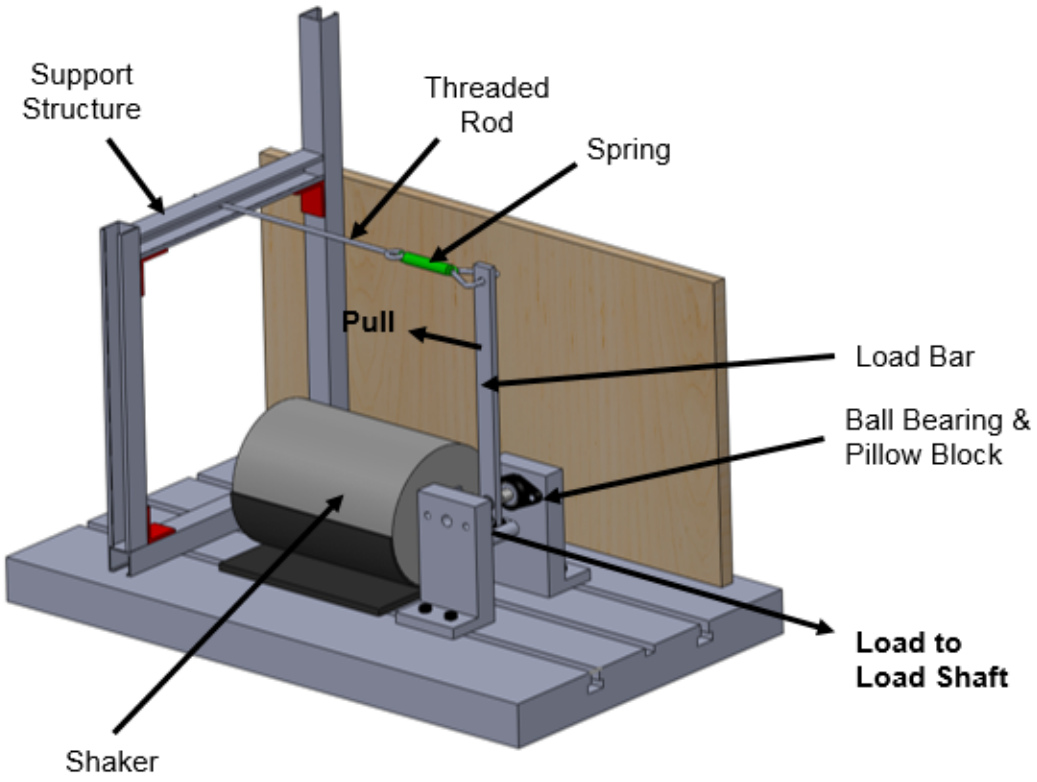

(a)

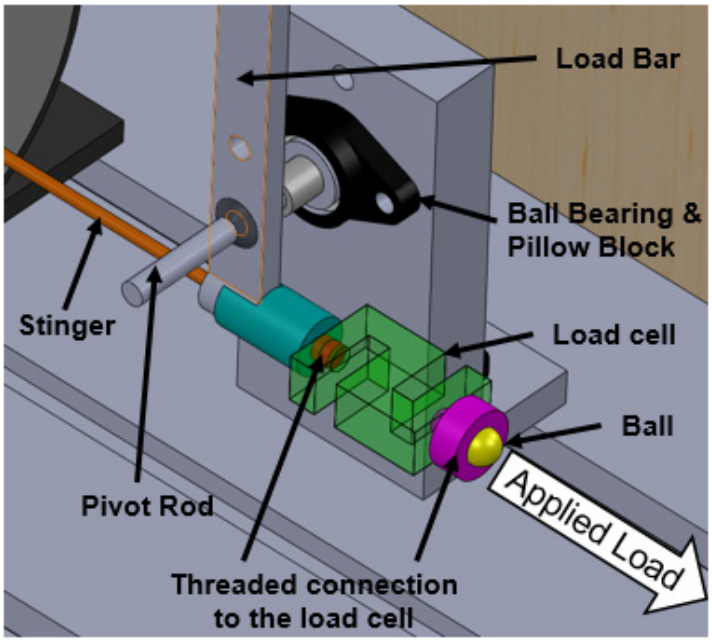

(b)

Figure 11. Isometric view of (a) static and dynamic load system and (b) load mechanism.

Instrumentation and Data Acquisition

Table 1 shows the instrumentation presently installed on the thrust bearing test rig. Four eddy current sensors measure the lateral position (X,Y) of each thrust collar, and three (x2) eddy current sensors measure the axial clearance at three angular locations on each thrust collar and relative to its respective thrust bearing. Each eddy current sensor is calibrated to stainless steel, yielding a sensitivity of ~10.2 V/mm, different from the vendor specified sensitivity to 4140 steel (~7.9 V/mm). A signal conditioner removes the bias voltage from the eddy current sensors so that their output range is within the acceptable limits of the data acquisition (DAQ) system (±10V).

Table 1. Instrumentation on the thrust bearing test rig.

Sensor Type	Quantity	Range
Eddy Current Sensor	10	0 – 2 mm
Turbine Flow Meter	3	0.25 – 25 GPM
Static Pressure Transducer	7	0 – 20.7 bar
Strain Gauge Load Cell	1	0 – 2200 N
Optical Tachometer	1	0 – 250 krpm
K-Type Thermocouple	1	0 – 100 °C
Signal Conditioner	12	1-1000X, ±10 V
LabView cDAQ	16	±10 V
	8	0 – 20 mA

There are seven static pressure transducers (strain gauge type. One measures the water supply pressure into each journal bearing, two other sensors measure the supply pressure into each half of the slave thrust bearing, the fourth sensor records the supply pressure into the test TB, a fifth the exhaust pressure, and the six and seventh sensor record the recess pressure of two pockets on the test TB. (Three) turbine flow meters measure the supply flow rate into the journal bearings, the supply flow rate into the test TB, and the exhaust flow rate through the inner diameter of the test TB.

A thermocouple measures the temperature of the water supplied to the test thrust bearing. A strain gauge load cell records the load applied by the static load system and the e-shaker onto the test TB. An optical tachometer measures the rotor speed. A LabView® program serves to acquire

and record voltages and currents from the various instrumentation. Other available DAQ systems include signal analyzers, and a Bentley Nevada ADRE © system.*

Rotor-Coupling Free-Free Mode Natural Frequencies and Shapes

Prior work shows that the test rotor and the quill-shaft coupling operate as a single unit and must be considered as such for a sound rotordynamic analysis. Appendix B describes the set-up and procedure for measuring the free-free mode natural frequencies and mode shapes of the rotor-coupling assembly. Table 2 and Figure 12 show the first three measured and (XLTRC^2) predicted free-free mode natural frequencies and shapes of the rotor-coupling assembly [12]. The predictions agree very well for the first two free-free mode shapes and natural frequencies are in close agreement with the test data.

Table 2. Measured and predicted free-free mode natural frequencies of rotor-coupling system.

	Measured Frequency [Hz]	Predicted Frequency [Hz]	Percent Difference
1st Free-Free Mode	104 ± 8	101	2.9
2nd Free-Free Mode	544 ± 8	555	2.0
3rd Free-Free Mode	1,280 ± 8	1,304	1.9

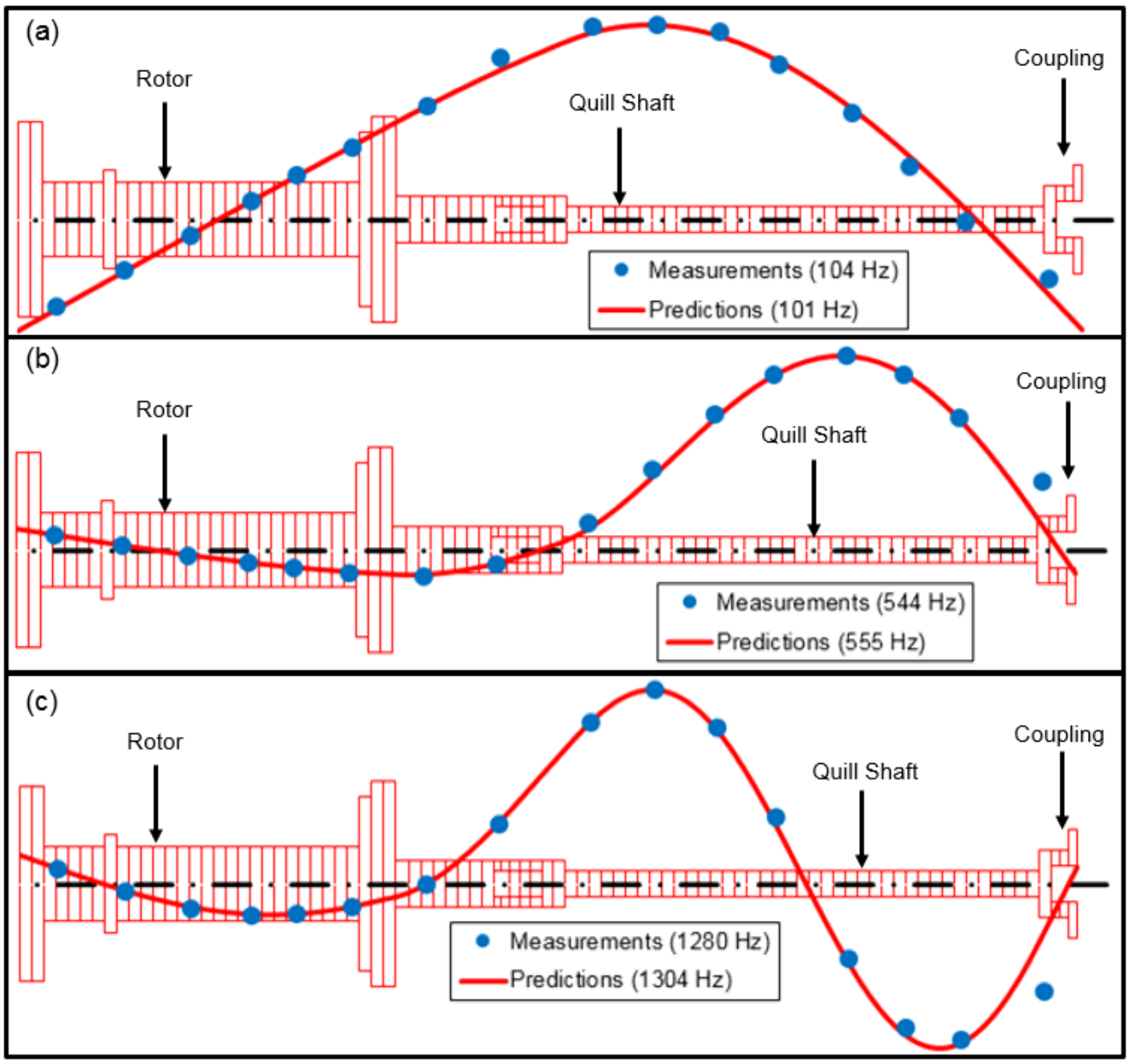

Figure 12. Measured and predicted (a) first, (b) second, and (c) third free-free mode shapes of the rotor-coupling system, respectively.

Impact Load Tests on Rotor-Coupling-Bearing System Operating without Rotor Speed

Apparatus and Procedure

With the rotor and coupling connected, water (24 °C) at 3.45 bar(g) the hybrid journal bearings and lifts the rotor-coupling system without either thrust bearing active. An impact hammer strikes the center of the quill shaft, causing the rotor coupling system to vibrate at the (rotor-coupling-radial bearings) system fundamental natural frequency.

Static pressure transducers and a turbine flow meter measure the supply pressure and flow rate into the journal bearings, respectively. Eddy current sensors measure the lateral displacement at each of the rotor thrust collars. A signal analyzer averages the displacement response in the frequency domain from 25 impacts. The frequency response and the half-power method aid to estimate the system natural frequency and damping ratio as the water supply delivered to the bearings increases.

Flow Rate vs. Water Supply Pressure into Radial Bearings

Figure 13 shows the flow rate of the water delivered to both journal bearings vs. the water supply pressure into each journal bearing. The figure includes predictions from XLHydroJet® [13], which are in agreement with the measured flow rate, showing the flow to increase as the pressure supply into the bearings increases.

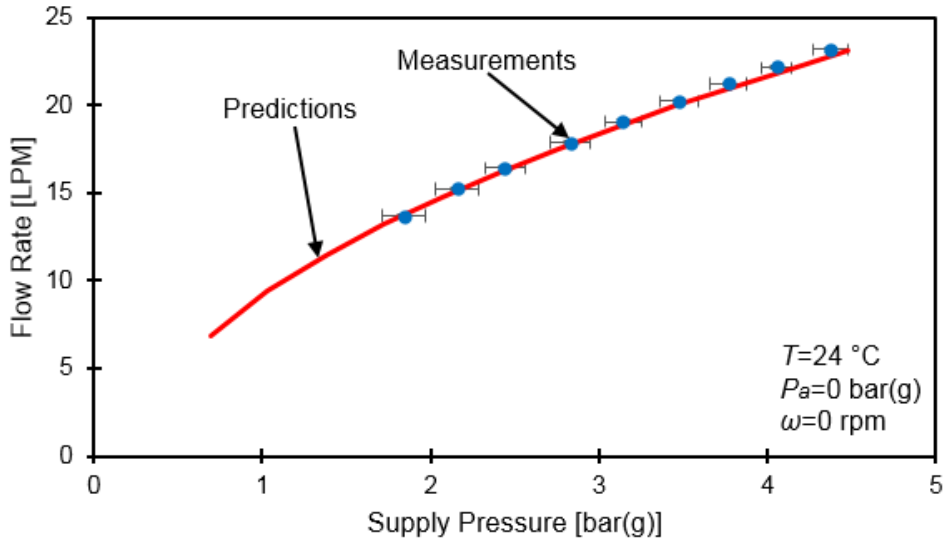

Figure 13. Measured and predicted water supply flow rate into both journal bearings vs. water supply pressure at room temperature (*T*=24 °C) for operation without rotor speed (Ω). Ambient pressure (P_a) is 0 bar(g).

Natural Frequency and Damping Ratio vs. Water Supply Pressure into Radial Bearings

Figure 14 shows the amplitude of rotor motion, normalized with respect to its peak amplitude, vs. frequency for operation with water (24 °C) supplied at 2.07, 3.45, and 4.83 bar(g) into the radial bearings. The ambient pressure is 0 bar(g). The rotor displacement is recorded at the thrust collar on the opposite side of the motor.

Table 3 lists the hydrostatic journal bearing operating characteristics and force coefficients calculated by XLHydroJet® [13]. Figure 15 shows the predicted fundamental mode shape of the

rotor-coupling assembly when water (24 °C) at 3.45 bar supplies the radial bearings. The inset table shows the relative amplitude and phase angle between measured displacements on each thrust collar corresponding to the predicted mode shape. The fundamental mode shape shows the quill shaft bending while the rotor displaces as a rigid body in conical motion.

Figures 16 and 17 show the fundamental natural frequency and system damping ratio versus supply water pressure into the radial bearings. The natural frequency only increases slightly from 91 Hz to 95 Hz as the water lubricant supply pressure increases from 2 bar(g) to 6 bar(g) because the flexibility of the quill shaft controls the natural frequency. The damping ratio is rather low because the highly flexible quill shaft has no external damping. Nonetheless, the damping ratio increases significantly from 4.8% to 6.8% as the water lubricant supply pressure increases from 2 bar(g) to 6 bar(g). Figures 16 and 17 also show XLTRC^2 structural model predictions obtained with bearing force coefficients supplied by XLHydrojet®, see Table 3.The predictions agree well with the measured natural frequency and identified damping ratio.

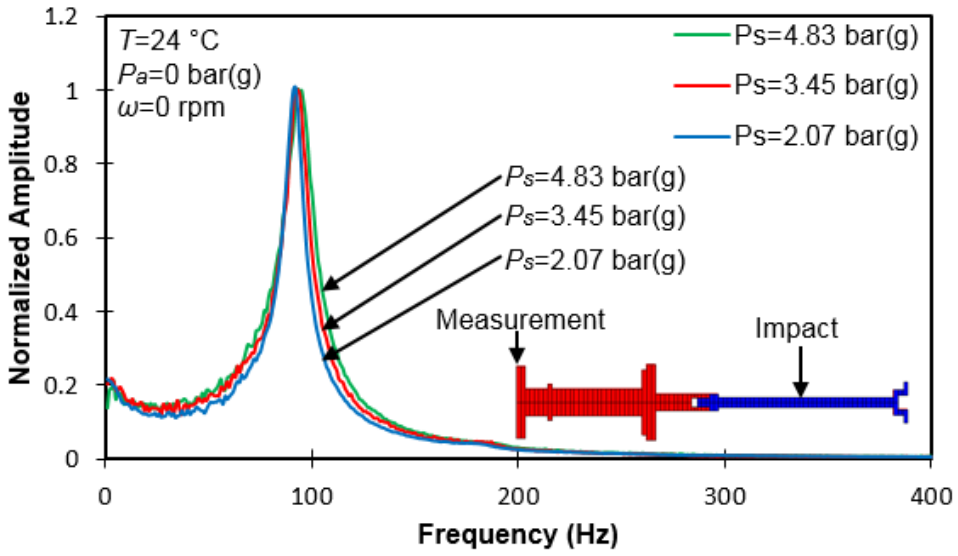

Figure 14. Amplitude of rotor motion, normalized with respect to peak amplitude, vs. frequency for operation without rotor speed, and with room temperature (*T*=24 °C) water at supply pressure (P_S) of 2.07, 3.45, and 4.83 bar(g). Ambient pressure (P_a) is 0 bar(g). Measurement at 45° away from vertical plane on free end thrust collar. Inset shows impact and measurement locations.

Table 3. Predicted journal bearing coefficients lubricated with water. Radial clearance = 89 μm. Pure hydrostatic operation. Model in Ref. [9]

Supply Pressure [bar (g)]	Static Eccentricity [μm]	Flow Rate [LPM]	Pocket Pressure [bar (g)]	Horizontal Direct Stiffness [MN/m]	Vertical Direct Stiffness [MN/m]	Horizontal Direct Damping [Ns/m]	Vertical Direct Damping [Ns/m]
1.38	23	5.7	0.86	0.81	0.81	720	760
2.07	18	7.4	1.06	1.10	1.10	800	820
2.76	14	8.8	1.26	1.33	1.33	870	880
3.45	13	10.0	1.44	1.52	1.54	940	950
4.14	11	11.0	1.62	1.69	1.71	1000	1000
4.83	10	12.0	1.81	1.85	1.87	1060	1070
5.52	9	12.9	2.00	2.01	2.02	1120	1120
6.21	9	13.7	2.20	2.16	2.17	1180	1180
6.89	8	14.5	2.38	2.31	2.32	1230	1230

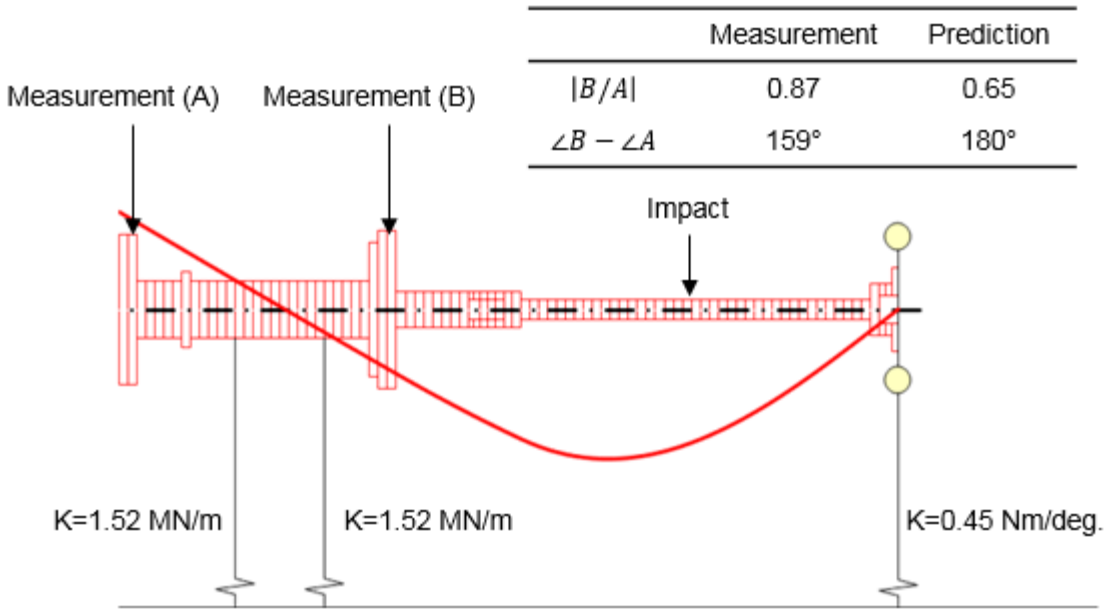

	Measurement	Prediction
$\lvert B/A \rvert$	0.87	0.65
$\angle B - \angle A$	159°	180°

Figure 15. Predicted mode shape of rotor-coupling at its fundamental natural frequency for operation without rotor speed. Water at 3.45 bar(g) and *T*=24 °C supplies the radial bearings. Ambient pressure is 0 bar(g). The relative amplitude ($|\boldsymbol{B/A}|$) and phase angle ($\angle \boldsymbol{B} - \angle \boldsymbol{A}$) between measured displacements on each thrust collar correspond to the predicted mode shape.

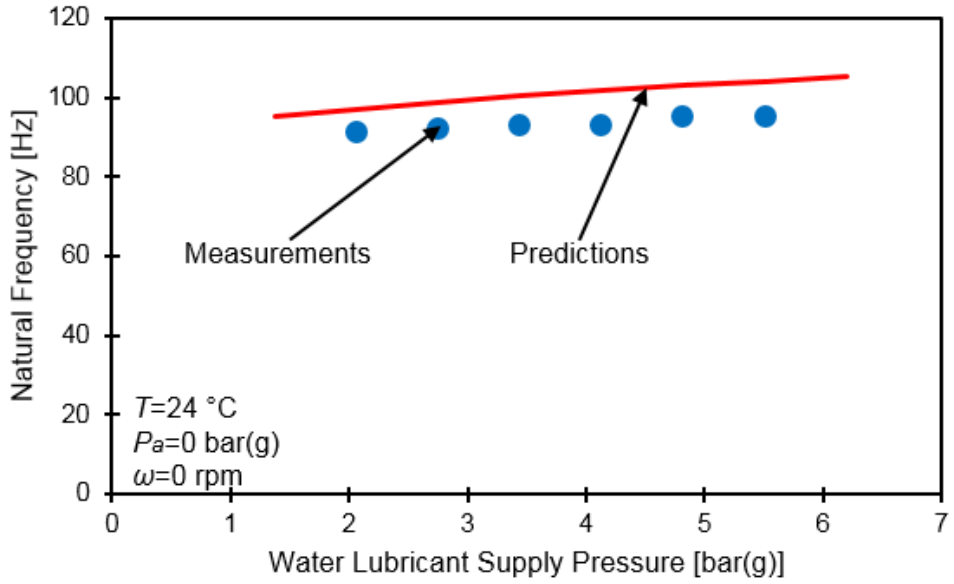

Figure 16. Measured and predicted natural frequency vs. water lubricant supply pressure into journal bearings. Water inlet temperature *T*=24 °C. Operation without rotor speed. Ambient pressure (P_a) is 0 bar(g). Uncertainty in natural frequency is ±1 Hz.

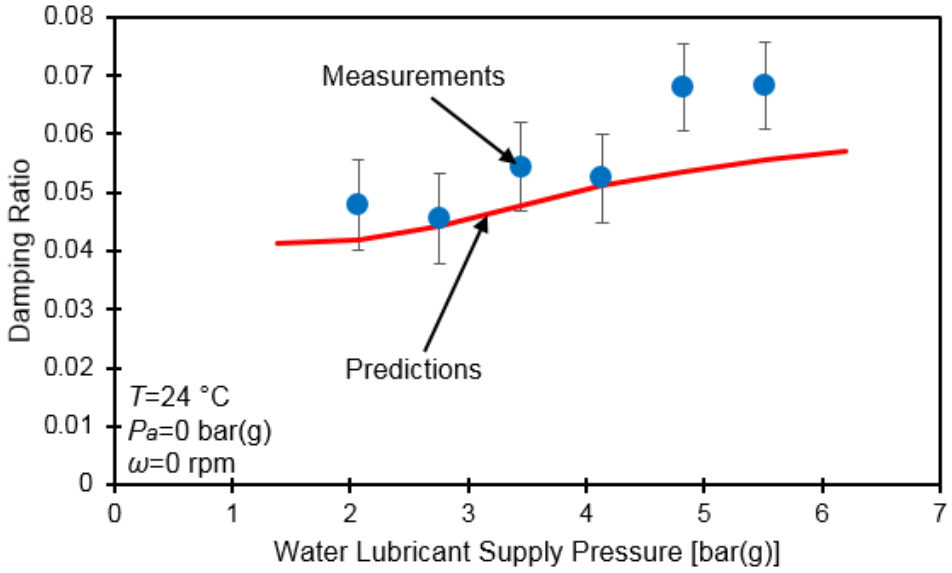

Figure 17. Measured and predicted damping ratio vs. water lubricant supply pressure into journal bearings. Water inlet temperature T=24 °C. Operation without rotor speed. Ambient pressure (P_a) is 0 bar(g). Damping ratio estimated using the half-power method. Error bars show uncertainty in damping ratio.

Thrust Bearing Performance for Tests without Rotor Speed

Table 4 and Figure 18 present the geometric characteristics and a depiction of the hydrostatic thrust bearings, respectively. Without shaft rotation, pressurized water at T=24 °C feeds the journal bearings at 3.45 bar(g). Water at an increasing pressure supplies both the test and slave thrust bearings (max. 4.14 bar(g)). The load shaft pushes the test thrust bearing towards the rotor causing the thrust bearing to push a load onto the rotor thrust collar. The slave thrust bearing, rigidly affixed to the housing, reacts to the applied load. Eddy current sensors face a thrust collar and measure the axial clearance at three circumferential locations. A pressure transducer measures the pressure (P_R) in a recess or pocket. At a constant lubricant supply pressure into the thrust bearings, the load incrementally decreases. The above procedure is repeated for water (24 °C) feeding the thrust bearings at a supply pressure (P_S) of 2.76, 3.45, and 4.14 bar(g).

Table 4. Dimensions and physical parameters of hydrostatic thrust bearings [10]. Material: 660 Bearing Bronze.

Thrust Face	Inner Diameter	40.64 mm
	Outer Diameter	76.2 mm
	Flange Outer Diameter	98.43 mm
Pocket	Number of Pockets	8
	Arc Length	20°
	Radial Length	8.13 mm
	Depth	444.5 μm / 508 μm
	Pocket/Wetted Area Ratio	0.19
Orifice (one per pocket)	Diameter	1.8 mm
	Radial Location	27.43 mm

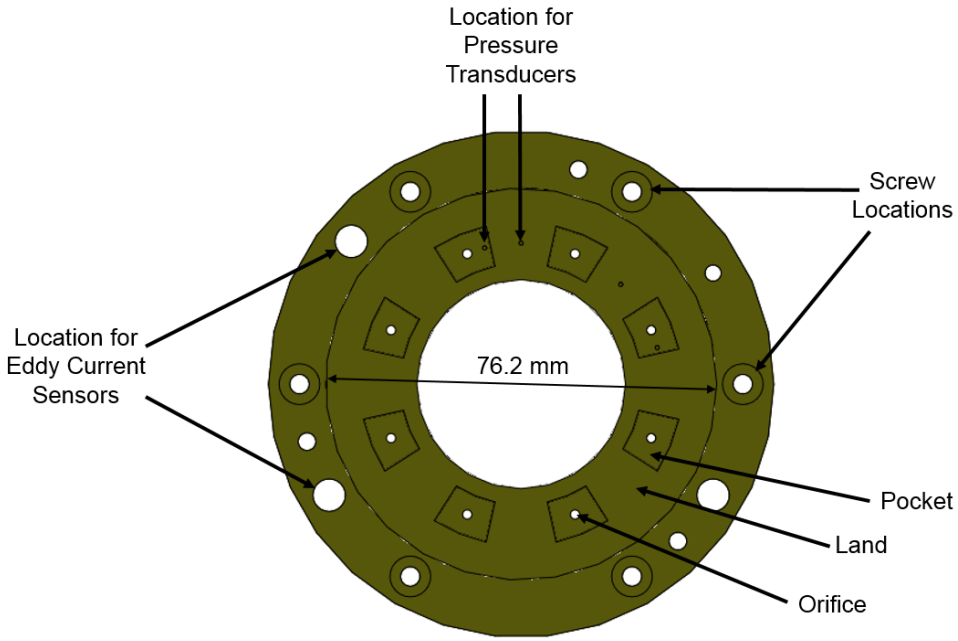

Figure 18. Depiction of water lubricated hybrid thrust bearing [10].

Clearance vs. Specific Load for Operation with Water at Various Supply Pressure and without Rotor Speed

For operation without rotor speed, i.e. pure hydrostatic, Figures 19 and 20 show the axial clearance of the TB versus applied axial load per unit area (W/A) and the pocket pressure ratio (P_R/P_S) versus axial clearance, respectively. Note A=32.6 cm^2 $= \frac{1}{4}\pi(D_O^2 - D_I^2)$. In both figures, water (24 °C) feeds the thrust bearings at a supply pressure (P_S) 2.76, 3.45, and 4.14 bar(g). The

exhaust pressure is ambient (P_a) = 0 bar(g). For a constant load, the axial clearance increases as the water lubricant pressure supply increases. However, the specific load (*W/A*) is only a fraction of the water lubricant supply pressure. At each lubricant supply pressure, the axial clearance decreases as the specific load increases. As the clearance decreases, the flow rate into the thrust bearings also decreases due to the increase in flow resistance across the film lands of the thrust bearings. As the flow rate decreases, the water lubricant has a lower pressure drop across the orifices of the TB, resulting in a higher pocket pressure. Thus, the pocket pressure ratio increases as the axial clearance decreases.

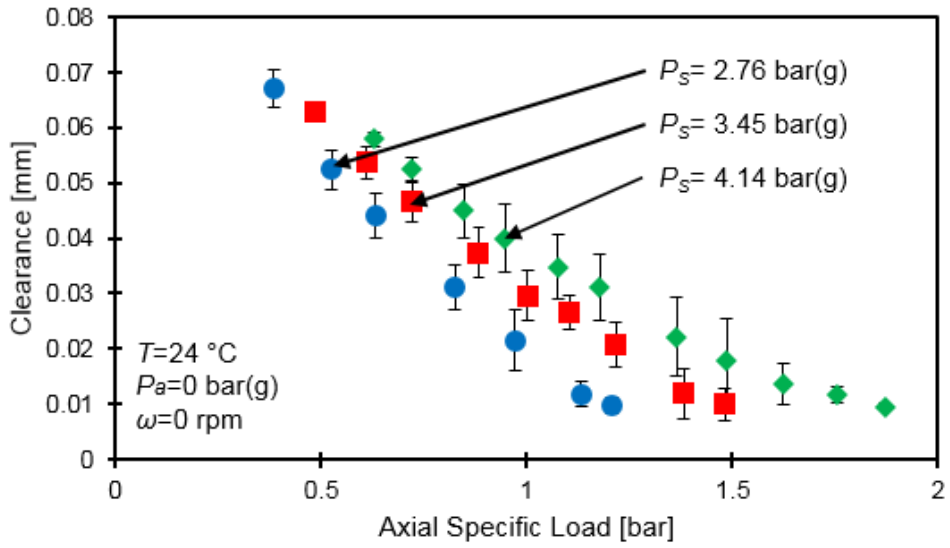

Figure 19. Axial clearance of thrust bearing vs. specific load (*W/A*) for operation with water (24 °C) at a supply pressure (P_S) of 2.75, 3.45, and 4.14 bar into the thrust bearings. No shaft rotation. Water at 3.45 bar(g) feeds the journal bearings. Ambient pressure (P_a) is 0 bar(g). Error bars indicate the minimum and maximum clearances on the face of the thrust bearing.

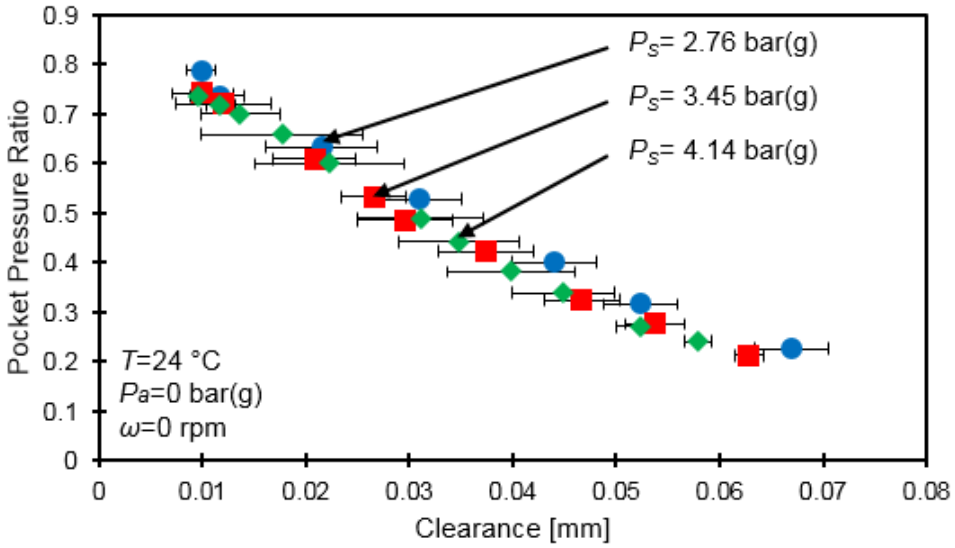

Figure 20. Pocket pressure ratio vs. axial clearance for operation with water (24 °C) at a supply pressure (P_S) of 2.76, 3.45, and 4.14 bar into the thrust bearings. No shaft rotation. Journal bearings operate with water at a supply pressure of 3.45 bar. Ambient pressure (P_a) is 0 bar(g). Error bars indicate the minimum and maximum clearance of the face of the thrust bearing.

Closure

After a catastrophic failure in 2013, the thrust bearing test rig, after extensive repairs, is operable with water as a lubricant. The rig is ready to provide reliable experimental results and to validate predictions. The end objective is to improve the design of thrust bearings. Previously, the same test rig showed remarkable correlation between predictions and experimental results for water lubricated hybrid thrust bearings [4].

This past year a number of modifications and enhancements were enacted. A diagnostic procedure with the original rotor showed that the thrust collars are not orthogonal with the shaft centerline. Hence, a new rotor was machined and balanced. A drill/tap process removed the remnant material from the housing, enabling the housing to hold air buffer seals and eddy current sensors. The refurbished water pipeline manifold has presently an increased pipe diameter to minimize frictional losses in the water as it flows to supply the bearings. The motor shaft centerline and rotor centerline are presently aligned within the coupling vendor's specifications using the face and rim alignment method. The design of a static load system enables the superposition of static and dynamic loads to excite the thrust bearing. The instrumentation is in place with multiple Eddy current sensors, various turbine flow meters, static pressure transducers, an optical tachometer, a strain gauge load cell, and a thermocouple. The sensor monitor the operating

conditions of the test rig. Presently, during its maiden operation, the revamped test rig operated at a rotational speed of 5 krpm.

Measurements of the free-free mode natural frequencies and mode shapes of the rotor-coupling assembly show that the rotor and quill shaft operate as a single unit, and hence must be considered as such for an accurate rotordynamic analysis. With the test rig completely assembled, water (24 °C) supplies the radial bearings at increasing supply pressure (max 6 bar(g)) for operation without rotor speed or active thrust bearings. Impact loads are exerted on the quill shaft, and lateral displacements of the rotor-coupling assembly help to identify the rotor-coupling-radial bearing system fundamental natural frequency and damping ratio. The natural frequency increases little (91 Hz to 95 Hz) as the water supply pressure increases (2 bar(g) to 6 bar(g)) because the flexibility of the quill shaft commands the placement of the natural frequency. The damping ratio is rather low because the flexible quill shaft has no external damping. However, the damping ratio increases significantly (4.8% to 6.8% as the water supply pressure increases (2 bar(g) to 6 bar(g)). XLTRC^2 predictions agree well with the measured natural frequency and identified damping ratio.

Without shaft speed, water at room temperature (24 °C) feeds the journal bearings at 3.45 bar(g) and the thrust bearings at increasing supply pressure (max. 4.14 bar(g)). At each water lubricant supply pressure into the thrust bearings, the test thrust bearing applies an incrementally decreasing load onto the rotor thrust collar. At a constant load, the axial clearance increases as the water supply pressure increases. However, the axial load per unit area [$A = \frac{\pi}{4}(D_O^2 - D_I^2)$] is only a fraction of the water pressure supplied to thrust bearings. At each water lubricant supply pressure, the axial clearance decreases as the applied axial load increases. The flow rate into the test thrust bearing decreases as the axial clearance decreases because of the increased flow resistance across the film lands. The relationship between clearance and flow rate results in a higher recess pressure at a lower axial clearance.

The main objective of the work for next year is to measure the performance of a hybrid thrust bearing (eight pocket) lubricated with water. The test rig could also be used to test other bearings with a 3-inch outer diameter at speeds up to 9 krpm. The first task will be to measure axial clearance vs. specific thrust load (max. 2.0 bar) over a range of rotor speed (max. 9 krpm) and bearing supply pressure (max. 6 bar). The second task will be to measure the axial response from perturbation loads over a range of rotor speed (max. 9 krpm), bearing supply pressure (max. 6 bar), thrust bearing clearance (min. 25 μm), and excitation frequency (max. 150 Hz). The final task is

to estimate the thrust bearing stiffness and damping coefficients based on the measured axial response.

References

[1] Rohmer, M., San Andrés, L., 2014, "Revamping a Thrust Bearing Test Rig," Annual Progress Report to the Turbomachinery Research Consortium, **TRC-B&C-03-2014**, *Turbomachinery Laboratory, Texas A&M University*, May.

[2] San Andrés, L., 2013, "A Test Rig for Evaluation of Thrust Bearings and Face Seals," TAMU Proposal to TRC, *Turbomachinery Laboratory, Texas A&M University*, May.

[3] Forsberg, M., 2008, "Comparison Between Predictions and Experimental Measurements for an Eight Pocket Annular HTB," M.S. Thesis, Mechanical Engineering, Texas A&M University, College Station, TX.

[4] Esser, P., 2010, "Measurements versus Predictions for a Hybrid (Hydrostatic plus Hydrodynamic) Thrust Bearing for a Range of Orifice Diameters," M.S. Thesis, Mechanical Engineering, College Station, TX.

[5] San Andrés, L., 2010, *Modern Lubrication Theory*, "Hydrostatic Journal Bearings," Notes 12b, Texas A&M University Digital Libraries, http://repository.tamu.edu/handle/1969.1/93197.

[6] Rowe, W., 1983, *Hydrostatic and Hybrid Bearing Design*, Textbook, Butterworths, pp. 1-20, 46-68.

[7] Sternlicht, B., Elwell, R.C., 1960, "Theoretical and Experimental Analysis of Hydrostatic Thrust Bearings," *ASME J. Basic Eng.*, **82**(3), pp. 505-512.

[8] San Andrés, L., 2000, "Bulk-Flow Analysis of Hybrid Thrust Bearings for Process Fluid Applications," *ASME J. of Trib.*, **122**(1), pp. 170-180.

[9] San Andrés, L., 2002, "Effects of Misalignment on Turbulent Flow Hybrid Thrust Bearings," *ASME J. of Trib.*, **124**(1), pp. 212-219.

[10] San Andrés, L., Phillips, S., and Childs, D., 2008, "Static Load Performance of a Hybrid Thrust Bearing: Measurement and Validation of Predictive Tool," 6th Modeling and Simulation Subcommittee / 4th Liquid Propulsion Subcommittee / 3rd Spacecraft Propulsion Subcommittee Joint Meeting. December 8-12, Orlando, Florida, JANNAF-120 Paper.

[11] Ramirez, F., 2008, "Comparison between Predictions and Measurements of Performance Characteristics for an Eight Pocket Hybrid (Combination Hydrostatic/Hydrodynamic) Thrust Bearing," M.S. Thesis, Mechanical Engineering, Texas A&M University, College Station, TX.

[12] XLTRC^2, 2002, Computational Rotordynamics Software Suite, *Turbomachinery Laboratory, Texas A&M University*.

[13] San Andrés, L., and Childs, D., 1997, "Angled Injection – Hydrostatic Bearings, Analysis and Comparison to Test Results," ASME J. Tribol., **119**, pp. 179-187.

[14] San Andrés, L., Rohmer, M., 2014, "Measurements and XLTRC^2 Predictions of Mass Moments of Inertia, Free-Free Natural Frequencies and Mode Shapes of Rotor and Flexible Coupling," Internal Progress Report, *Turbomachinery Laboratory, Texas A&M University,* March.

Appendix A: Description of TAMU Thrust Bearing Test Rig [10]

Figure 21 depicts a cross sectional view of the test rig designed and constructed to measure the static and dynamic forced performance of a (water lubricated) hydrostatic thrust bearing. Figure 22 shows a three-dimensional exploded view of the major components in the test rig. A motor drives the test rotor through a quill coupling (not shown). The test rotor is a long shaft with two thrust collars at its ends. Two flexure pivot type radial hydrostatic bearings support the test rotor, whose center of mass is located between the two radial bearings. Ref. [3] provides full details on the design of the major components of the test rig.

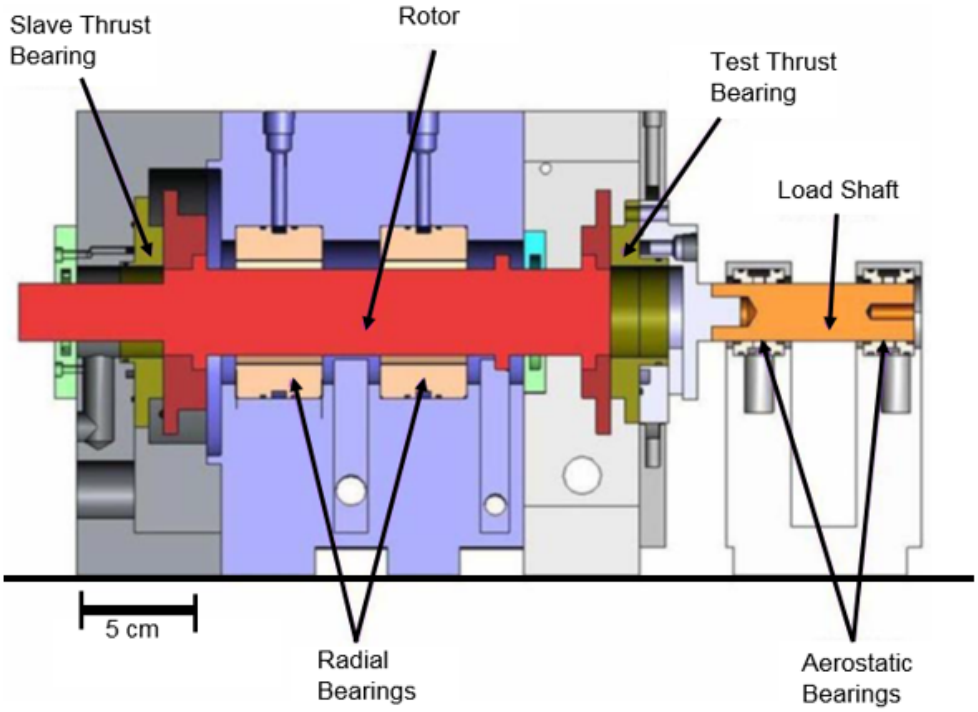

Figure 21. Cross sectional view of hydrostatic thrust bearing test rig [10].

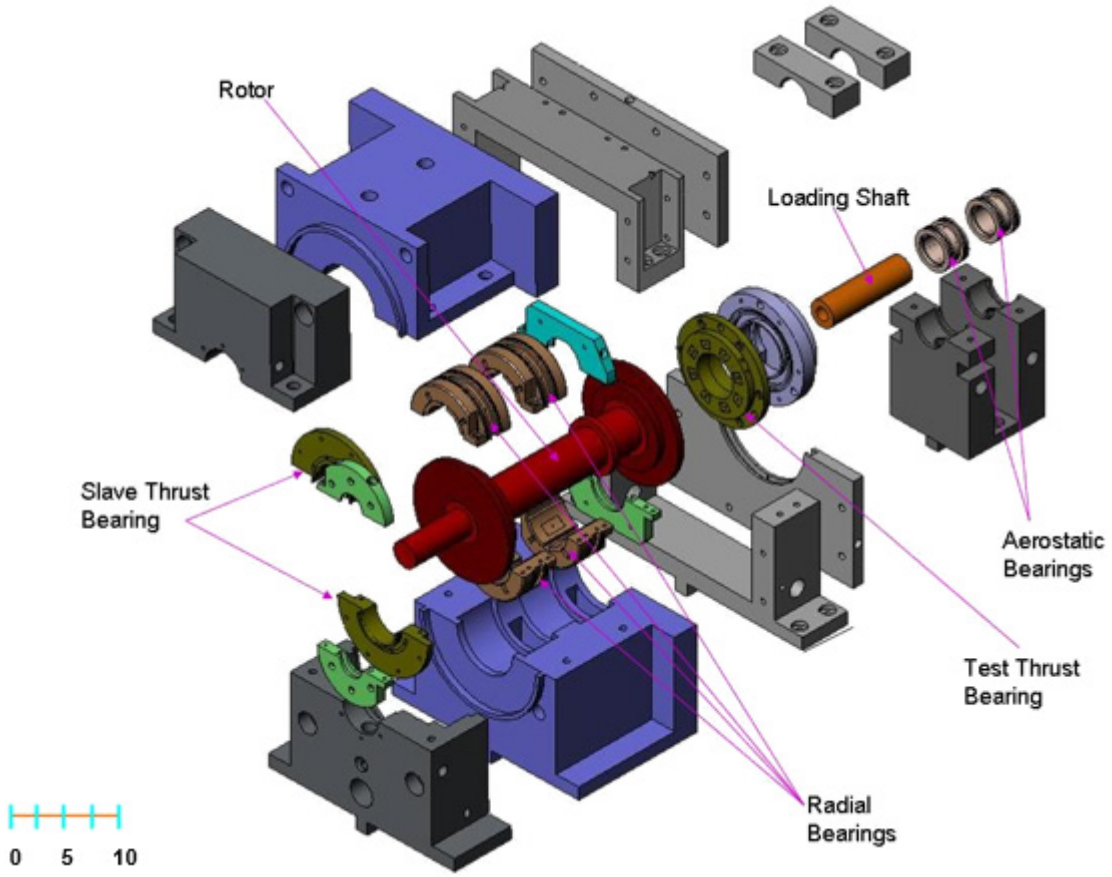

Figure 22. Exploded view of hydrostatic thrust bearing test rig (Units: cm) [10].

The test rig has two water lubricated hydrostatic thrust bearings; one is the test bearing (on the right of Figure 21) and the other is a slave bearing, both facing the outer side of the thrust collars on the rotor. The slave thrust bearing is affixed rigidly to a bearing support, as shown on the left of Figure 21. A loading system (not shown), through a non-rotating shaft, delivers an axial load (static and/or dynamic) to the test thrust bearing. Two aerostatic radial bearings support the axial load shaft with minimal friction for motions in the axial direction. The test thrust bearing, depicted on the right of Figure 21, moves axially to impose a load on the rotor thrust collar. This axial load is also reacted by the slave thrust bearing. Consult Figure 22 for the following description. Upon assembly, the rotor is first mounted on the bottom halves of the radial bearings. Next, the top and bottom halves are fastened to each other, and O-rings are installed on the bearings' outer diameters. The rotor and radial bearing assembly is then placed into the bottom part of the radial bearing housing. The top part of the housing is then fastened to its bottom and feed and discharge water lines connected.

Figure 23 depicts a schematic view of the test rig with its bearings as mechanical elements providing stiffness and damping for load support and energy dissipation, respectively. The rotor comprises a 19.7 cm long 316 stainless steel shaft with two thrust disks (collars). The shaft diameter at the location of the radial bearings is 38.1 mm, while the thrust collars have an outer diameter equal to 108 mm. The radial hydrostatic/hydrodynamic bearings, see Figure 24, are made of Bronze 330 and manufactured with a wired EDM process to render a flexure pivot – tilting pad type bearing (to avoid potential hydrodynamic instability induced by shaft rotation). The bearings are split in half for ease of installation. The radial bearing length and inner diameter equal 38.1 mm, with a machined radial clearance of 0.089 mm. A bearing has four 72° arc pads with 60% pivot offset and 20% nominal preload. Each pad contains a pocket recess for hydrostatic pressurization. The pocket dimension are 12.7 mm width, 24° arc extent, and 0.508 mm depth. The orifice for lubricant injection into the bearing is radial and at the center of a recess area. The ratio of pocket area to pad wetted area is 11% in accordance with accepted design practices for cryogenic liquid bearings. The pocket depth may seem excessive, but consider the lubricant is warm water (25 °C). Hence, pneumatic hammer effects are of no importance in the current test rig. This is not the case if a pressurized gas, air for example, is the working fluid in the bearings.

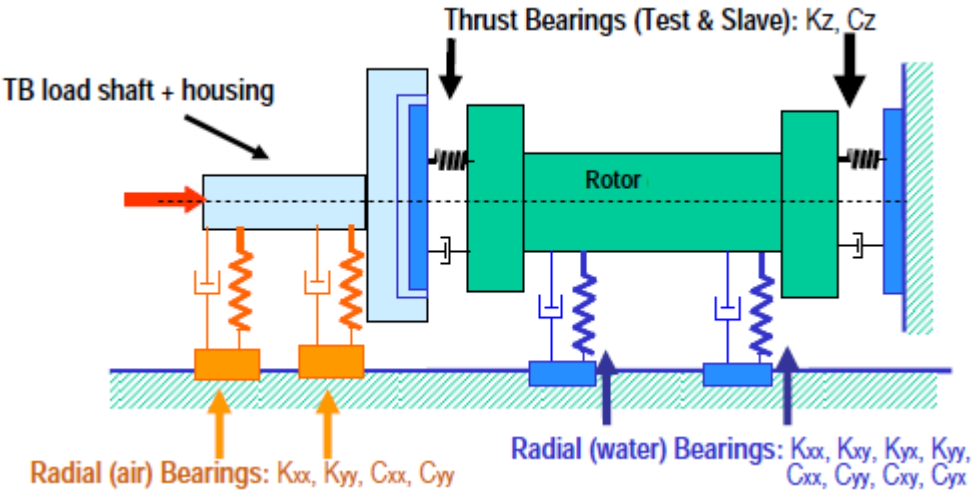

Figure 23. Schematic representation of test rig: thrust and radial bearings as mechanical elements with stiffness and damping characteristics [10].

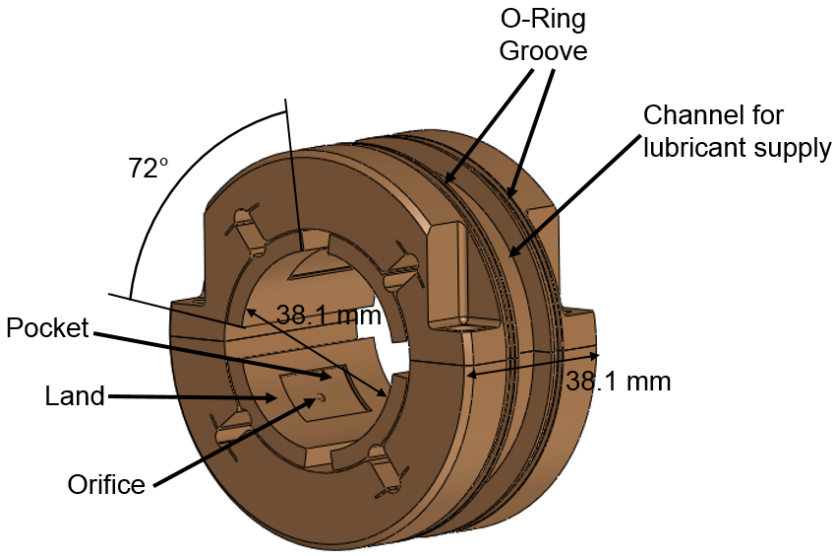

Figure 24. Depiction of water lubricated flexure pivot pad hydrostatic journal bearing [10].

Figure 25 depicts the test hydrostatic thrust bearing. The slave bearing is identical to the test bearing, except that it is machined as two mating halves for ease of installation. The bearings have flat faces with inner and outer diameters equal to 40.6 and 76.2 mm, respectively. Each bearing has eight pockets, 20° arc length and 8.13 mm in radial length, uniformly distributed on the bearing circumference. The center of a pocket is located at a diameter of 54.86 mm, i.e. non-coinciding with the bearing mid-diameter (58.42 mm), to reduce the spurious effects of centrifugal flow at high rotational speeds. The orifice injection is axial, i.e. perpendicular to the faces of the thrust bearing.

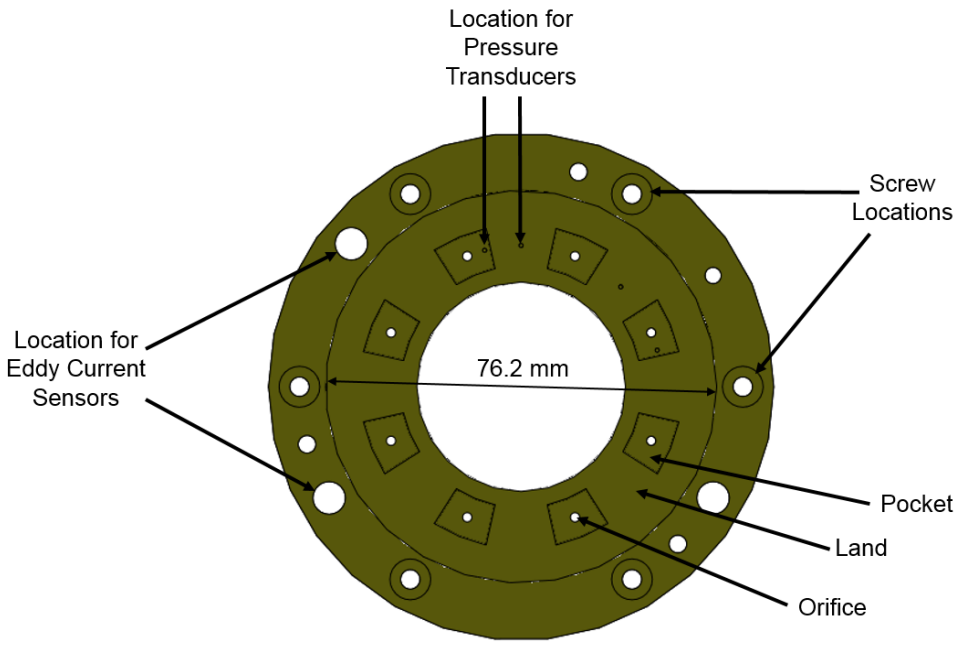

Figure 25. Depiction of water lubricated hybrid thrust bearing [10].

The electric drive motor is rated at 22 kW at a maximum operating speed of 30 krpm. The motor can deliver a constant torque, maximum 700 N-cm, over the entire speed range. A digital closed-loop speed control and a water chiller for cooling are included. The coupling is a flexible element with quill shaft and a hub clamp. The coupling has a maximum speed rating of 30 krpm and 93.2 N-m continuous torque. In addition, the coupling has a very low axial stiffness (3.5 N/mm) with an allowance of 0.61 to 1.22 mm axial travel. These characteristics permit isolating the motor from the axial loads imposed on the thrust bearings.

Appendix B: Procedure for Measuring Free-Free Mode Shapes and Natural Frequencies [14]

Figure 26 shows the (ad-hoc) set up to measure the free-free mode natural frequencies and mode shapes of the rotor-coupling assembly. Two inextensible strings suspend the rotor-coupling assembly. The strings provide negligible stiffness in the direction orthogonal to their length. Wax affixes two 1 gram piezoelectric accelerometers to the rotor. One reference accelerometer remains stationary on the assembly, while the other accelerometer roams to various positions on the rotor-coupling assembly.

An impact hammer strikes the rotor-coupling assembly and excites it. The dynamic signal analyzer records the amplitude of acceleration, the natural frequency, and the phase angle between the two accelerometers. The dynamic signal analyzer averages the response of twenty-five impulses. Wax affixes the roaming accelerometer to nineteen other locations, and the process listed above is repeated. The relative amplitudes and phase angles between the two accelerometers at different locations determine the mode shape at each natural frequency.

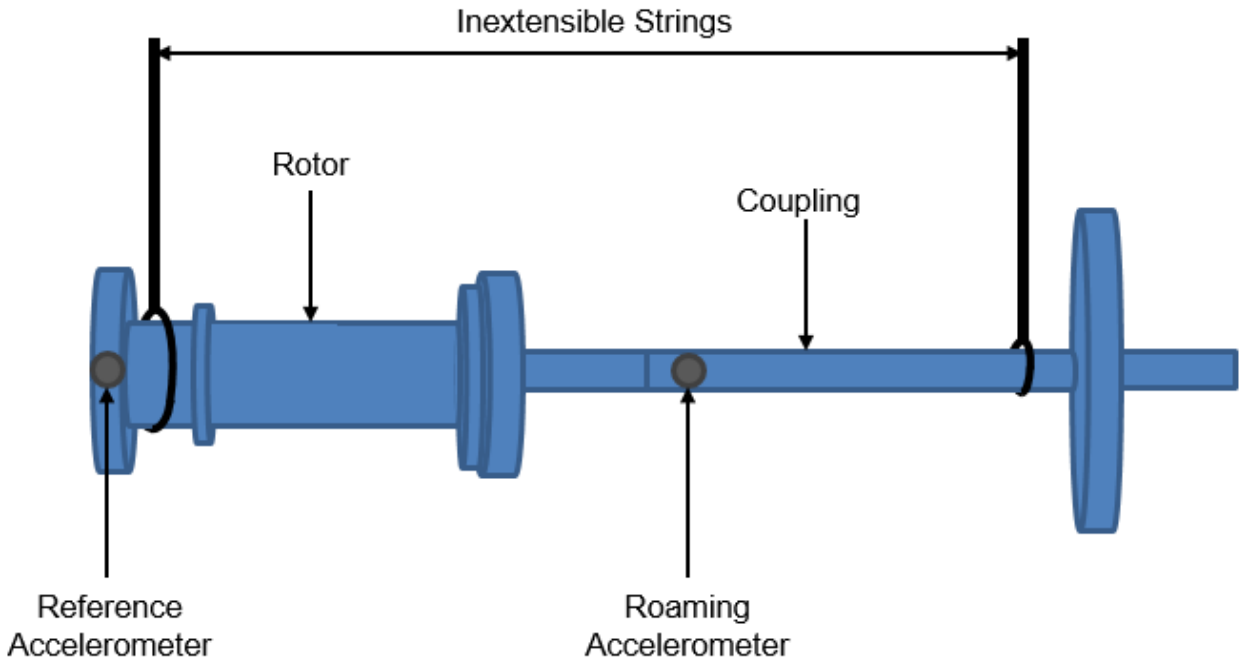

Figure 26. Schematic view of rotor-coupling assembly suspended with two accelerometers mounted to measure free-free mode natural frequencies and mode shapes of the system.